Seasonal and Interannual Variability in a Hybrid Coupled GCM

HSIN-HSIN SYU AND J. DAVID NEELIN

Department of Atmospheric Sciences, University of California, Los Angeles, Los Angeles, California

DAVID GUTZLER

NOAA Aeronomy Laboratory, Boulder, Colorado

(Manuscript received 9 February 1994, in final form 19 December 1994)

ABSTRACT

A hybrid coupled model for the tropical Pacific ocean–atmosphere system is used to simulate El Niño–Southern Oscillation (ENSO) interannual variability and to investigate the role of coupling in the seasonal cycle. An ocean GCM (OGCM) is coupled to an empirical atmospheric model that specifies a wind stress field from a given sea surface temperature (SST) field. The stress is estimated by singular value decomposition of the covariance between observed surface wind stress and SST fluctuations. Two versions of the atmospheric model are employed: one includes only spatial patterns of the atmospheric feedbacks associated with interannual variability, whereas the other also includes spatial patterns associated with the annual cycle. In the latter version, wind stress coupling in the seasonal cycle is modeled on the same basis as in the interannual variability. The seasonal cycle enters through prescribed heat flux and is modified by momentum-flux feedbacks. In the OGCM, two vertical mixing schemes—Philander–Pacanowski (PP) and a modified scheme—are used.

Simulated ENSO anomalies have a reasonable spatial structure compared to observations, and the form is not strongly sensitive to the atmospheric model or mixing scheme. SST anomalies evolve largely as a standing oscillation, though with some westward propagation; heat content evolution is characteristic of subsurface memory, consistent with a mixed SST–ocean dynamics mode regime. In the absence of the seasonal cycle, the ENSO period is affected by vertical mixing: about 2.3 years for the modified scheme and slightly less than 2 years for the PP scheme. Indications of irregular or multifrequency behavior are also found. Interaction with the seasonal cycle frequency locks the interannual signal to a quasi-biennial period. The seasonal cycle in the eastern Pacific is well simulated by the coupled model. Wind stress feedbacks are an important part of the cycle near the equator but are not the sole factor in producing westward propagation along the equator. The seasonal cycle in the western Pacific shows great sensitivity to the mixing scheme. With the PP scheme, small errors in the uncoupled simulation are amplified by coupling; with the modified scheme, great improvements are obtained. These differences also provide an example of nonlinear interaction between ENSO and the coupled seasonal cycle. With the PP scheme, the amplitude of the ENSO signal increases with coupling, but at strong coupling competition with ENSO can decrease the amplitude of the seasonal cycle in the cold tongue region. However, with the modified scheme, although the irregularity of interannual variability is increased, stronger coupling does not affect the amplitude of the coupled seasonal cycle in equatorial SST. Simulating the seasonal cycle on the same basis as interannual variability thus provides much stronger constraints on subgrid-scale parameterizations than simulating ENSO alone.

1. Introduction

Coupled ocean–atmosphere models of several levels of complexity have been developed to study tropical ocean–atmosphere interactions, especially the El Niño–Southern Oscillation (ENSO) phenomenon. These include simple models (e.g., Philander et al. 1984; Gill 1985; Hirst 1986; Neelin 1991), intermediate coupled models (e.g., Cane and Zebiak 1985; Anderson and McCreary 1985; Battisti 1988; Schopf and Suarez 1988), hybrid coupled general circulation models (Neelin 1990; Latif and Villwock 1990), and coupled general circulation models (e.g., Mechoso et al. 1995; Latif et al. 1993a,b; Philander et al. 1992). The class of "hybrid coupled models" (HCMs) consists of an ocean GCM (OGCM) coupled to a simplified atmospheric model, which represents the steady-state atmospheric response to oceanic boundary conditions. This design makes use of the fact that the ocean is the important source of memory for the coupled system, and the atmosphere can be effectively treated as the "fast," adjusted component. For the tropical domain, temporal variability in the system is therefore due primarily to the coupling. This aids an understanding of the inherent properties of the coupled system in the absence of stochastic forcing by noncoupled variability. The hybrid model presented here is of a type first in-

Corresponding author address: J. David Neelin, Department of Atmospheric Sciences, University of California, Los Angeles, 405 Hilgard Avenue, Los Angeles, CA 90024.
E-mail: neelin@atmos.ucla.edu

troduced by Latif and Villwock (1990), which makes use of an empirical atmospheric component. Several other such models are currently being developed (Barnett et al. 1993; M. Flügel 1993, personal communication), all of which are based on the assumption that for monthly or longer timescales, contemporaneous correlation between wind stress and SST is associated with the atmosphere's rapidly adjusted response to the SST pattern nonlocally throughout the basin.

In addition to the role of ocean–atmosphere coupling in producing interannual variability, there are indications that aspects of the seasonal cycle in the tropical Pacific are strongly influenced by such feedbacks. For example, the seasonal maximum and minimum of SST and zonal wind stress have a tendency to propagate westward along the equator (Horel 1982). Several studies have postulated interactions between the annual and interannual timescales (e.g., Rasmusson and Carpenter 1982; Wallace et al. 1989; Meehl 1990). The onset of the El Niño events, for instance, tends to coincide with the warm phase of the seasonal cycle. We present here an approach to modeling coupled feedbacks in the seasonal cycle on the same basis as in the interannual variability. In particular, the "momentum feedbacks," that is, those due to the wind stress response to SST anomalies, are estimated for the departure of the seasonal cycle from annual average in addition to interannual anomalies.

This approach provides an additional challenge to the coupled model compared to simulation of the interannual variability about a fixed seasonal cycle. Our purpose is to understand the role of coupling within the seasonal cycle and the relationship between seasonal and interannual timescales. More detailed description of this coupling approach is provided in section 2. The empirical atmospheric model and OGCM are described in sections 3 and 4, respectively. Section 5 analyzes the results of "coupled seasonal cycle" experiments, in which both seasonal cycle and interannual variability are concurrently simulated. The inherent interannual variability in the absence of the seasonal cycle is addressed in section 6 to compare with that in the coupled seasonal cycle experiments. Sensitivity studies are presented in section 7. In each section, effects of two vertical mixing schemes upon coupled feedbacks in ENSO and seasonal simulations are examined.

2. Coupling approach

a. Heat flux parameterization

The atmospheric component includes both parameterization of heat flux and momentum feedbacks. The surface heat flux parameterization as formulated by Oberhuber (1988) includes observed heat flux [as estimated from the Comprehensive Ocean–Atmosphere Data Set (COADS) data] and a linearized negative feedback term $Q_{\text{model}} = Q_{\text{obs}} - \alpha(T_{\text{model}} - T_{\text{obs}})$, where α is the negative feedback coefficient, Q represents the net heat flux into the ocean, and T denotes SST. The magnitude of this negative feedback coefficient, resulting from the tendency of fluxes out of the ocean surface to increase with increasing SST, is important to the behavior of the system. In Oberhuber's calculation, this coefficient is estimated using bulk formulae for evaporation, sensible heat, etc. and taking the partial derivative with respect to SST assuming that atmospheric quantities do not vary with SST. Most importantly, the change of the atmospheric boundary layer moisture with SST is neglected, resulting in a considerable overestimate of the negative feedback. To resolve this problem, we use the same linearized form as Oberhuber and his values for the observed heat flux but with the negative feedback coefficient recalculated according to Seager et al. (1988). This parameterizes the atmospheric boundary layer moisture as following SST at a given fraction δ of the saturation value $q_{\text{sat}}(\text{SST})$.

The dependence of solar radiation on SST through cloudiness is neglected in the negative feedback term, but partial derivatives of latent heat flux, sensible heat, and longwave radiation are included. The latent heat flux is computed from the standard formula using a fixed subsaturation factor $\delta = 0.73$, chosen to match the average over the tropical Pacific domain. A drag coefficient $C_D = 1.2 \times 10^{-3}$ is used and a minimum wind speed of 4.5 m s^{-1} is imposed, acting as a parameterization for the contribution of high-frequency wind excluded in the monthly COADS wind speed data. The sensible and longwave radiative heat losses are combined and approximated as contributing a constant value of 1.5 W m^{-2} K^{-1} to the negative feedback coefficient. Outside the Tropics (beyond 20°N and 20°S), Seager's negative feedback coefficient is gradually blended with Oberhuber's estimate. A map of our negative feedback coefficient and relevant equations are presented in appendix A. Within the tropical Pacific basin, the horizontal distribution is consistent with both Oberhuber's and Seager's parameterizations, with lower magnitudes appearing mainly in the warm pool region along the western boundary and the cold tongue area along the eastern boundary. In both areas, the values estimated using Seager's formula, approximately −20 W m^{-2} K^{-1}, are about one-half of Oberhuber's calculation.

The modification of the negative feedback term with Seager's scheme reduces the damping effect of the fluxes, which tends to restore model SST toward an equilibrium temperature $T_0 = T_{\text{obs}} - \alpha^{-1}Q_{\text{obs}}$. The reduction of the negative feedback can be significant to the instability and equilibrated amplitude of interannual oscillations. However, due to the reduction of the negative feedback in the warm pool region, where the ocean model is unable to transport the heat flux as estimated by Oberhuber, the smaller negative feedback coefficient tends to result in higher SST. Relative to schemes that fix the atmospheric boundary layer temperature and moisture, and thus essentially fix SST,

this heat flux scheme allows much more freedom for SST. In seasonal cycle simulations, seasonal information enters the heat flux through Q_{obs} and T_{obs}, with α being fixed at its annual-average value.

b. *Momentum feedbacks: Seasonal versus interannual*

The empirical atmospheric model describes a linear nonlocal relationship between wind (pseudo-) stress anomalies and SST anomalies, estimated from observations using a singular value decomposition (SVD) technique as described in section 3. The fundamental assumption is that the causal relation producing these correlations is due to the atmospheric response to SST boundary conditions; this is based on results of both simple atmospheric models and atmospheric GCMs, and relies on the separation of adjustment timescales between ocean and atmosphere. In coupling, an SST anomaly pattern from the ocean model is projected onto the SST component of the stress–SST modes. The corresponding wind stress anomaly pattern is then reconstructed, multiplying the pseudostress by an atmospheric density $\rho_a = 1.27$ kg m^{-3} and using a drag coefficient $C_D = 1.2 \times 10^{-3}$. The stress anomalies are further multiplied by a scalar parameter—the relative coupling coefficient—before being added to the climatological wind stress field to force the ocean again. This procedure is carried out at a coupling interval (1 day for all runs described here) over which SST is averaged before the reference state (discussed below) is subtracted to produce the next SST anomaly. Coupling is active only in a domain from 20°S to 20°N.

Two versions of the atmospheric model were estimated. In the principal version, anomalies are defined with respect to the long-term annual average. The atmospheric model thus attempts to include the annual cycle response of the winds to SST in addition to interannual anomalies; we refer to this version as SVDAI hereafter. The wind stress patterns associated with the seasonal cycle are assumed to be forced by the seasonal cycle of SST anomalies (i.e., departures from annual average). This is reasonable over most of a basin the size of the Pacific, although there is some risk of attributing to SST winds forced by continental effects near the coasts. The second version, referred to as SVDI, uses anomalies defined with respect to the mean seasonal cycle and thus models only the wind response to SST typical of interannual anomalies. The coupled response to both these versions is compared in some cases without seasonal cycle to estimate the effects of the two approaches on the simulation of interannual variability.

In the runs described here, coupling is carried out in two ways. For experiments without the seasonal cycle, standard one-way flux correction is used: a climatological stationary point is created by defining SST anomalies with respect to a "seasonless" ocean climatology, that is, the response to prescribed annual-average stress and heat flux (i.e., Q_{obs}). For experiments with the seasonal cycle, the heat flux is specified as a function of season, but the specified climatological winds are seasonally invariant and the seasonless ocean climatology still serves as the reference state in defining SST anomalies. The seasonal cycle of winds is produced through the SVDAI model response to changes in SST; in other words, the momentum feedbacks are fully coupled processes. This approximates the realistic situation where the seasonal cycle enters through the solar component of the heat flux, and the winds and ocean respond in a coupled manner. Here, the net observed heat flux is specified, so we can isolate the role of the momentum feedbacks in the coupled seasonal cycle. Both seasonal and interannual timescales are included and can interact in this type of experiment.

3. Estimation of empirical atmospheric models

The empirical atmospheric models used in this study are estimated using SVD of the covariance matrix calculated from the time series of pairs of observed monthly mean fields. The objective of each model is to determine statistically optimized coupled modes of variability that can be used to define a field of wind stress, using as input a field of SST anomalies. Two versions are estimated as referred to in section 2. For the SVDAI model, both annual and interannual responses of winds to SST are retained. The SVDI model is derived from the same data but with the annual cycle removed before calculating covariances between grid-point time series.

a. *Data*

Observed monthly mean SST and surface pseudostress data τ, for the 19-yr period from January 1970 through December 1988, are used to derive the empirical atmospheric model. The SST data were analyzed at the U.S. National Meteorological Center using both in situ and satellite observations (Reynolds 1988). The τ vector fields were subjectively analyzed at The Florida State University (Legler and O'Brien 1984). For this study, both SST and τ fields have been averaged onto a 187-point grid with 4° lat × 8° long resolution covering the tropical Pacific basin between latitudes 20°N and 20°S.

We denote SST fields as $T_i(t)$ and zonal and meridional components of the vector pseudostress as $u_i(t)$ and $v_i(t)$, where i denotes a particular grid point and t is a particular month. The two stress components at each grid point are treated as independent scalar variables for this analysis by combining the u and v fields for each month into a single field $w_j(t)$. This treatment is less efficient in terms of variance capture than a more general complex analysis of stress vectors (Legler 1983), but comparison of EOFs derived from separate

scalar components (not shown) with Legler's vector EOFs suggests that the differences are probably not significant.

b. *Singular value decomposition*

Singular value decomposition operates on the matrix C_{ij}, whose elements are the covariances between T_i and w_j (i.e., $C_{ij}(T, w) = \langle T_i w_j \rangle$, where the brackets denote a time average over all 228 months). In the SVDAI model, the 19-yr climatological annual mean values of T and w are subtracted from each gridpoint value before taking the cross product; in the SVDI model, 19-yr climatological means for each calendar month are first removed. Neither model attempts to capture the spatial structure of the long-term (annual) mean, which is prescribed from the data.

As discussed in detail by Bretherton et al. (1992), the eigenvectors $\mathbf{T}_k$ of the matrix CC^T (where the superscript T denotes the transpose operator and the subscript k is a mode number) and the eigenvectors $\mathbf{w}_k$ of the matrix C^TC are called the singular vectors of the T and w fields, respectively. The first k eigenvalues of CC^T and C^TC are equal and nonzero ($k = \min(i, j)$, in this case 187) and are called the singular values; we denote them σ_k^2, ranked in the usual order from largest to smallest. The singular values represent the squared covariance accounted for by each pair of singular vectors.

The projection of T on $\mathbf{T}_1$ has the maximum covariance with the projection of w on $\mathbf{w}_1$ relative to any possible pair of patterns $\mathbf{T}$ and $\mathbf{w}$. The projections of succeeding pairs of singular vectors $\mathbf{T}_k$ and $\mathbf{w}_k$ have the maximum *covariance* relative to any possible pair of patterns that are orthogonal to the preceding singular vectors. In this sense, the SVD model defines an empirically optimized set of coupled modes. For comparison, canonical correlation analysis (CCA) [used by Graham et al. (1987) and Barnett et al. (1993) in other statistical studies of coupled ocean–atmosphere variability across the tropical Pacific] optimizes the *correlation* between patterns of variability. For the tropical SST and stress fields considered here, either optimization criterion effectively describes patterns of large-scale variability similar to those derived from EOF analysis applied to either field separately, and the results are not sensitive to the choice of CCA or SVD. Nigam and Shen (1993) have applied rotated principal component analysis of combined fields in a similar context.

The time series of expansion coefficients (denoted θ or ω) associated with each singular vector is the projection of the vector ($\mathbf{T}$ or $\mathbf{w}$) onto the time series of fields (T or w) associated with it, analogous to the expansion coefficients associated with EOFs. We then divide θ_k and ω_k by their respective standard deviations and multiply the singular vectors by the same quantities. Thus, the time series of expansion coefficients becomes unit normal variates and the gridpoint values of the singular vectors are dimensionalized with units of SST (K) and pseudostress ($m^2\ s^{-2}$).

The first 20 singular values for the SVDAI and SVDI models are plotted in Fig. 1. The first singular value of the SVDAI model is associated with the 12-month harmonic and is far off scale; subsequent singular values are more comparable to the SVDI model. The sequence of singular values is used to determine the number of modes to retain in the model; typically one cuts off retention at an empirically determined mode number beyond which the variance (or in this case covariance) drops off sharply, as in the "scree test" of Cattell (1966) or the "shelf test" of O'Lenic and Livezey (1988). Such dropoff points can be seen after modes 1, 2, 3, and 7 of the SVDAI series; modes 8–20 seem to belong to a "continuum" of explained covariance, which may be plausibly interpreted as noise. In the SVDI series, no obvious dropoff point is seen beyond mode 1. From consideration of the sequence of SVDAI singular values and examination of the eigenvectors, we chose to include the first seven coupled modes for each model.

The coupled model results from projecting a monthly mean T field (an observed field or one produced by an ocean model) onto the first seven SST singular vectors to derive an empirical estimate of w. Because the expansion coefficients have been normalized, θ_k and ω_k have the same amplitude and the relationship between the two is optimally given by $\omega_k(t) = \theta_k(t)$. Estimating a stress field from an SST field involves the following steps:

1) Project T onto the first SVD mode of SST ($\mathbf{T}_1$) to obtain a dimensional value of θ_1.
2) Normalize θ_1 through division by the variance of T associated with mode k.
3) Relate θ_1 to ω_1 by $\omega_1 = \theta_1$.
4) Multiply the first SVD mode of stress $\mathbf{w}_1$ by ω_1 to obtain w_1.

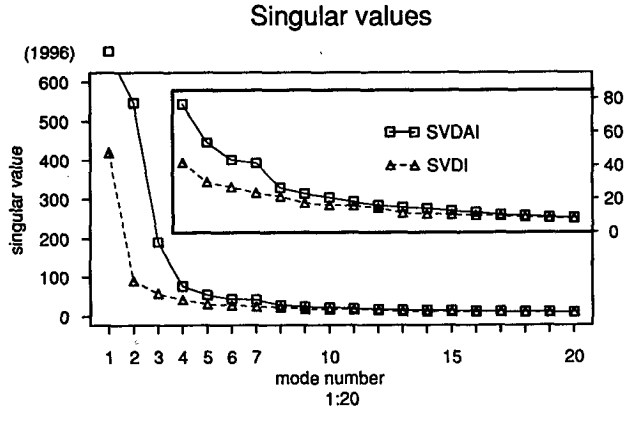

FIG. 1. Singular values of modes 1–20 of the SVDAI analysis (squares) and the SVDI analysis (triangles), units K $m^2\ s^{-2}$. The first singular value of SVDAI has a value of 1996 K $m^2\ s^{-2}$, which is far off scale. The inset plot reproduces the singular values for modes 4–20 on an expanded ordinate scale, shown along the right-hand side.

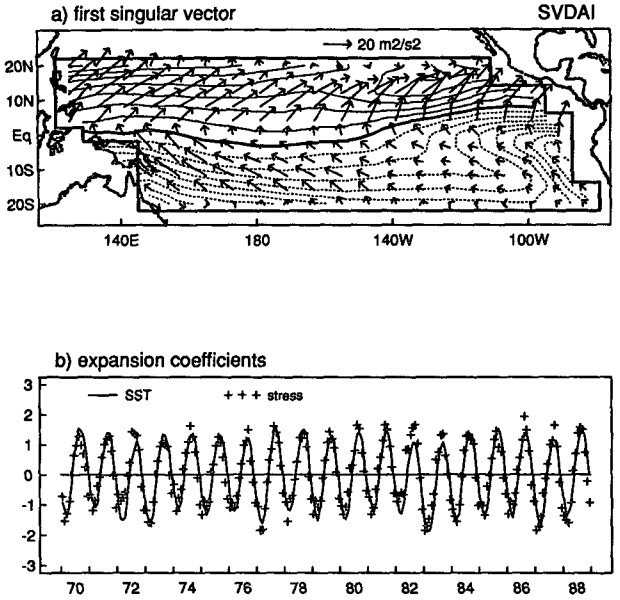

FIG. 2. Spatial patterns and time series associated with the first mode of the SVDAI model. (a) Dimensional patterns of SST and stress derived from the first pair of singular vectors. Contour interval for SST is 0.2°C, with negative contours dashed and the zero contour plotted extra thick. Scale for stress vectors is shown at the top of the plot. (b) Nondimensional expansion coefficients for the patterns shown in (a); SST time series plotted as a solid line, stress time series plotted as crosses.

5) Repeat steps 1–4 for subsequent modes.

6) The orthogonality of the modes implies that the total field w is the sum $w_1 + w_2 + \cdots + w_7$.

c. *SVDAI and SVDI model results*

Averaged over the entire domain of active coupling (equatorward of 20°), slightly less than 40% of the zonal stress variance, and about half of the meridional stress variance, is accounted for by fluctuations of SST in the SVDAI model. Considering only variability with periods greater than 1 year, however, the stress variance yielded by the SVDAI model is almost 80% of that observed, and averaged over just the grid points within 10° of the equator the SVDAI stress fields exhibit over 90% of the variance of the observations. Thus, the reduction from the observed stress variance in the SVDAI(θ) stress fields is mostly due to the removal of subannual, off-equatorial fluctuations. At least some of this uncoupled stress variability may be a result of errors in the subjectively analyzed stress fields across regions of poor sampling (Zebiak 1990), but it seems likely that much of the variance not captured by the SVD technique is real and represents the considerable fraction of stress variability that is not coupled (linearly) to SST fluctuations.

The SVDI model captures almost the same amount of low-frequency variance as the SVDAI model but yields less subannual variance. Thus, both SVD models effectively act as low-pass filters for the stress anomalies by passing only the stress variance coupled to the relatively slow-changing SST field.

Maps of the first three SVDAI dimensionalized singular vectors of SST and stress and their associated nondimensional expansion coefficients are shown in Figs. 2, 3, and 4. The first pattern pair (Fig. 2) describes an annual cycle (12-month harmonic) in SST and stress, as shown by the expansion coefficients. In the western half of the basin (west of about 150°W), $\mathbf{T}_1$ and $\mathbf{u}_1$ (the zonal component of the first stress mode) both exhibit annual cycles approximately symmetric about the equator with warm T and eastward u in local summer in both hemispheres; the amplitude of $\mathbf{T}_1$ in the west increasing monotonically poleward, and $\mathbf{u}_1$ exhibiting maximum amplitude at about 10°N and 10°S. In the eastern half of the basin, the annual cycle of the cold tongue along and just south of the equator is captured by $\mathbf{T}_1$ and the seasonal movement of the intertropical convergence zone (ITCZ) is described by $\mathbf{v}_1$, the meridional component of the first stress mode. Almost half the total SST variance is accounted for by the stress component of mode 1; a smaller fraction (roughly one-third, slightly more for v and slightly less for u) of the variability of the stress fields is accounted for by fluctuations of SST. Almost none of the variance of SST or zonal stress near the equator is associated with this mode.

The second pattern pair (Fig. 3) has combined characteristics, describing the component of the annual cycle in quadrature with mode 1 and also describing

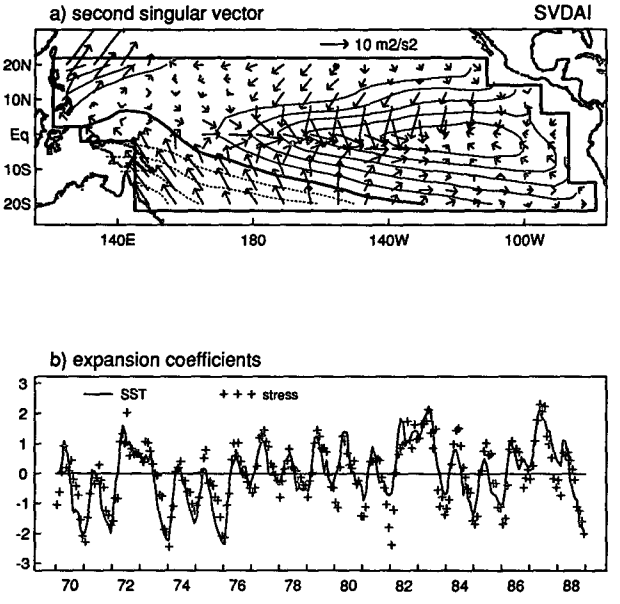

FIG. 3. As in Fig. 2 but for the second mode of the SVDAI model. Contour interval for the SST pattern is 0.2°C (as in Fig. 2a), but the scale for the stress vectors is halved compared with Fig. 2a.

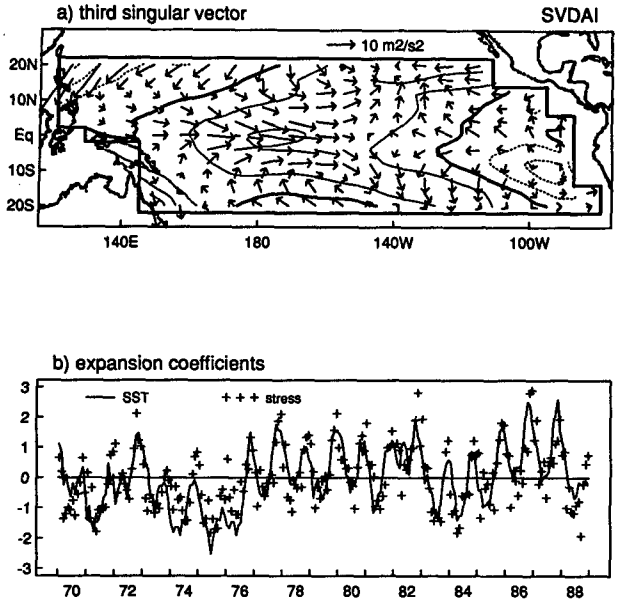

FIG. 4. As in Fig. 3 but for the third mode of the SVDAI model.

interannual fluctuations associated with El Niño. The pattern of T_2 shows an equatorially centered, zonally elongated anomaly extending eastward from the date line with maximum amplitude offshore at 110°W. Warm events (El Niño) are characterized by the absence of the seasonal oscillation of the expansion coefficients from positive to negative values in midyear in 1972, 1976, 1982, and 1986–87. The positive phase of T_2 (warm water on the equator) is coupled to eastward stresses in $\mathbf{u}_2$ over the western half of the warm water patch and weak westward stresses east of the T_2 SST maximum; that is, zonal stress anomalies converge onto the SST maximum (the model is linear so all signs are reversible). Meridional (southward) stress anomalies similar in amplitude to the eastward anomalies are directed across the SST anomaly gradient north and west of the SST anomaly center. The meridional anomalies south of the equator are weaker but still convergent.

The third pattern pair (Fig. 4) describes a broad SST fluctuation centered on the equator at the date line, with a smaller center (in terms of both spatial extent and amplitude) near the American coast. Mode 3 tends to lag mode 2 by a few months, indicating the known propensity for the phase of the seasonal cycle (and El Niño anomalies) to propagate westward. The spatial phase relationship between T and u along the equator in this mode is different than that found in mode 2: here the (eastward) zonal stress anomalies lie right on top of the (warm) SST anomalies. The meridional stress anomalies converging onto the equator in either hemisphere are only half as large as the zonal anomalies. Almost half of the SST variance at the equator and date line is accounted for by ω_3, and almost half of the zonal stress variance along the equator between about 160°W and 160°E is accounted for by θ_3.

Each of the first three modes of the SVDAI model contains a prominent annual cycle, indicating that the annual cycles of SST and stress cannot be captured by a single standing oscillation (or even two): a result consistent with previous diagnostic studies showing that the amplitude and phase of the seasonal cycles of SST and stress vary considerably across the tropical Pacific (Horel 1982). The blending of annual cycle and El Niño anomalies is consistent with many studies that have demonstrated that the latter tend to be phase-locked with respect to the former (Rasmusson and Carpenter 1982).

Modes 4–7 (not shown) are typically smaller in scale and have higher-frequency temporal variability. Mode 4 contains a prominent semiannual fluctuation, and modes 6 and 7 describe other near-equatorial anomaly patterns (capturing variance in regions where the local amplitudes are small in the higher-order modes).

Figures 5 and 6 show maps of the first two singular vectors of the SVDI model. Mode 1 of the SVDI model is very similar to mode 2 of the SVDAI model within 10° of the equator (compare Fig. 5a with Fig. 3a). The expansion coefficients associated with this mode, with the seasonal cycle now removed, track the temporal fluctuations of the Southern Oscillation index. Mode 2 (Fig. 6) reaches its largest amplitude during the 1982–

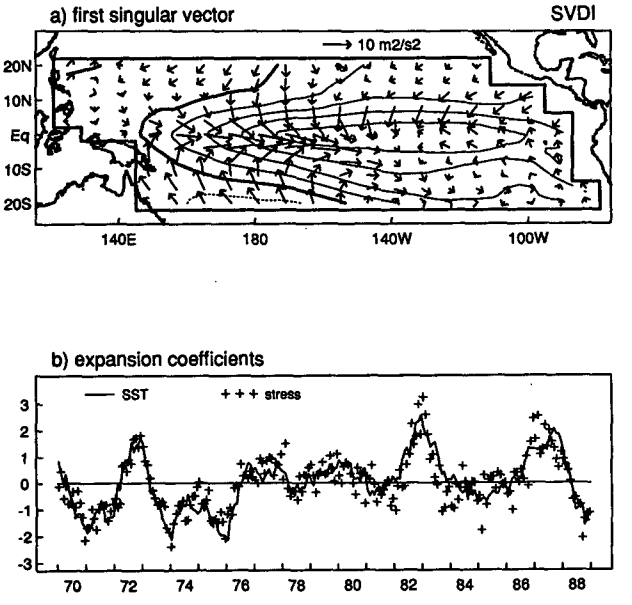

FIG. 5. Spatial patterns and time series associated with the first mode of the SVDI model. (a) Dimensional patterns of SST and stress anomalies derived from the first pair of singular vectors. Contour interval for SST is 0.2°C, with negative contours dashed and the zero contour plotted extra thick. Scale for stress vectors is shown at the top of the plot. (b) Nondimensional expansion coefficients for the patterns shown in (a); SST time series plotted as a solid line, stress time series plotted as crosses.

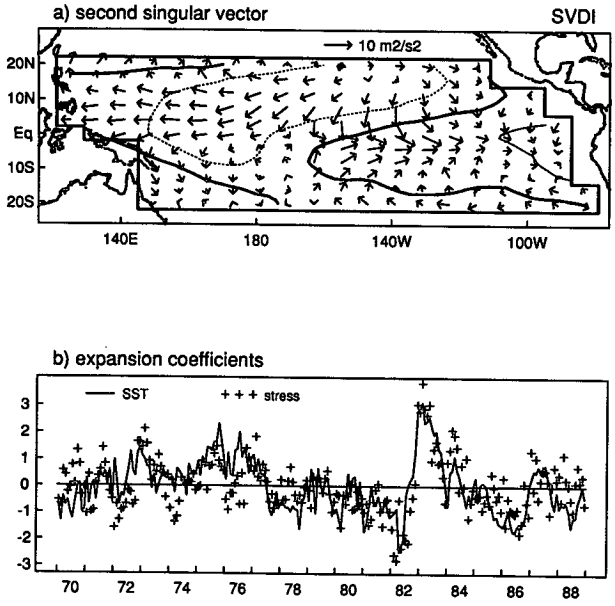

FIG. 6. As in Fig. 5 but for the second mode of the SVDI model.

83 warm event and describes a dipole of SST and zonal stress anomalies, with anomalies of SST and u of one sign to the east of 160°W and the opposite sign to the west of 160°W. The expansion coefficients of the stress component exhibit a weak but identifiable biennial spectral peak (Gutzler 1993); the biennial tendency is most pronounced in the 1970s when no comparable signal exists in the SST expansion coefficients.

We emphasize that in the coupled model, only the spatial patterns associated with the singular vectors are important: the atmospheric component produces the stress patterns shown in response to the SST patterns shown. No time domain information comes from the atmospheric model.

4. Ocean model simulation

The ocean component used in this study is a version of the Geophysical Fluid Dynamics Laboratory Modular Ocean Model (R. Pacanowski, K. Dixon, and A. Rosati 1991, personal communication), a 3D primitive-equation GCM based on Cox (1984). The ocean domain covers the Pacific basin from 30°S to 50°N, 130°E to 80°W with continents. To resolve equatorial waves, the ocean model has 0.5° latitude spacing in the equatorial region between 10°S and 10°N. The spacing is increased smoothly to 4° at the southern boundary and 5.6° at the northern boundary. Longitudinally, the mesh spacing varies from approximately 1° near the western boundary (chosen to resolve western boundary currents) to 3° in the central and eastern Pacific. A sponge layer is applied at the northern and southern boundaries of the domain to prevent climate drift from occurring during integration. Vertical resolution of 27 levels is used, with 10 levels in the upper 100 m. For the vertical mixing scheme, two versions are applied in the OGCM: the Richardson-number-dependent vertical mixing scheme of Philander and Pacanowski (1980, PP scheme hereafter) and a modified version of the PP scheme, developed by B. Blanke (1993, personal communication; modified scheme hereafter). In this paper, the modified scheme is used as our default.

In the PP scheme, vertical diffusivity and eddy viscosity were tuned to reproduce many characteristics of the equatorial Atlantic and Pacific, such as the mixed layer depth, the zonal slope of the thermocline, and the structure of the equatorial undercurrents, in the context of boundary conditions that strongly constrain SST. However, the use of this physics leads to some deficiencies in the reproduced uncoupled or coupled seasonal cycle. In an attempt to attenuate these problems, a new formulation for the dependence of diffusivity and viscosity on the local Richardson number has been tested by B. Blanke. These relationships mimic the results obtained by Peters et al. (1988) in their direct measurements of equatorial oceanic turbulence and the results obtained by Blanke and Delecluse (1993) with a more sophisticated turbulence closure scheme. The new formulation allows larger mixing in high turbulent regions and smaller mixing in low turbulent areas than the PP scheme. The modified scheme also implements an algorithm for the penetration of solar radiation over the first tens of meters in the ocean. An application of the modified vertical mixing scheme with the solar penetration is adopted in Waliser et al. (1995).

The OGCM is spun up from rest, with the initial temperature and salinity profiles of the Levitus (1982) climatology for January. After 3 years of integration, the upper ocean has approximately reached an equilibrium state in the case with the PP scheme. A longer run is necessary in the case with the modified scheme to fully equilibrate the ocean to avoid climate drift in the further coupled integrations. Three integrations for 9 years are made under different prescribed upper-boundary forcings: 1) annual-average stress and heat flux, 2) seasonal-varying stress and heat flux, and 3) annual-average stress and seasonal-varying heat flux.

The ocean climatology is defined as the average over the last year of the OGCM integration in which the model ocean is driven by seasonless forcing (the annual-average stress and heat flux). This serves as a reference state for defining anomalies in the coupled runs. Since the modified mixing scheme generates more mixing in the mixed layer, the ocean climatology has a deeper mixed layer in the west and weaker upwelling compared with the PP scheme. Overall, the spatial pattern of each field is reasonable compared with observations. Detailed description and figures of the ocean climatology in the case with the modified scheme are presented in appendix B.

For comparison with the coupled simulation of the seasonal cycle, a second OGCM integration is made with seasonally varying wind-stress and heat-flux boundary conditions. The seasonal cycle is calculated as the month-by-month mean for the last 4 years of a 9-yr run. We use the term "mean seasonal cycle," or MSC, in both coupled and uncoupled experiments, and will most often discuss this in terms of anomalies with respect to the annual average.

Figure 7a presents the SST anomalies of the MSC, repeated twice, as a function of time and longitude along the equator. Both amplitudes and positions of the maximum SST anomalies except for the weaker negative anomaly in the eastern Pacific are surprisingly close to observations, with a peak-to-peak difference of 3.5°C around 100°W, slightly away from the coast. An annual cycle is clearly seen with positive anomalies appearing from January to July in the eastern Pacific, but with a one-month shift compared with observations. Negative anomalies occur during the rest of the year and last longer than positive anomalies near the eastern coast. Extrema in the eastern Pacific occur during spring and fall. The westward propagation of SST anomalies in the central and eastern Pacific is also well simulated, but is less pronounced than in observations. In addition, both of the surface zonal current and upwelling anomalies (figures not shown) have a clear seasonal cycle, reflecting the seasonal variations of surface wind forcing. Off the equator, seasonal features in SST (figures not shown) are in good agreement with observations.

The same analysis for the above-mentioned integration with the second boundary condition but with the PP scheme is shown in Fig. 7b. Although both runs share many similar features, a striking difference between Figs. 7a and 7b is the appearance of excessive SST anomalies in the western Pacific in the run with the PP scheme. The modified scheme gives a better westward propagation but less successful simulation in amplitude for the cold anomalies in the eastern Pacific.

A measure of the impact of the seasonal variation of momentum flux to the ocean is provided by the difference between two OGCM simulations with the second and third boundary conditions: seasonal-varying stress and heat flux, and annual-average stress with seasonal-varying heat flux, respectively. The difference between both runs may be roughly interpreted as the component of the seasonal cycle that is forced by the seasonal variation of stress; however, the negative feedback term in the heat flux parameterization tends to reduce this difference by damping toward the seasonal cycle of SST. Thus, this difference should be taken as a conservative estimate of the impact of seasonal stress variations. The horizontal distribution of the SST difference between these two runs is shown in Figs. 8a–d after taking seasonal means. The impact of the seasonal variation of surface wind stress is mostly over the equatorial central and eastern Pacific in the equatorial cold tongue and coastal regions, mainly in the areas where dynamical mechanisms strongly affect SST. The patterns of wind stress departures from annual average that create the response in Fig. 8 closely resemble those given in Halpert and Ropelewski (1989). The largest signal is in the region just north of the equator, associated with movements of the ITCZ. The importance of the annual cycle of meridional wind stress is reflected in the substantial antisymmetric component of the SST pattern it forces on either side of the equator.

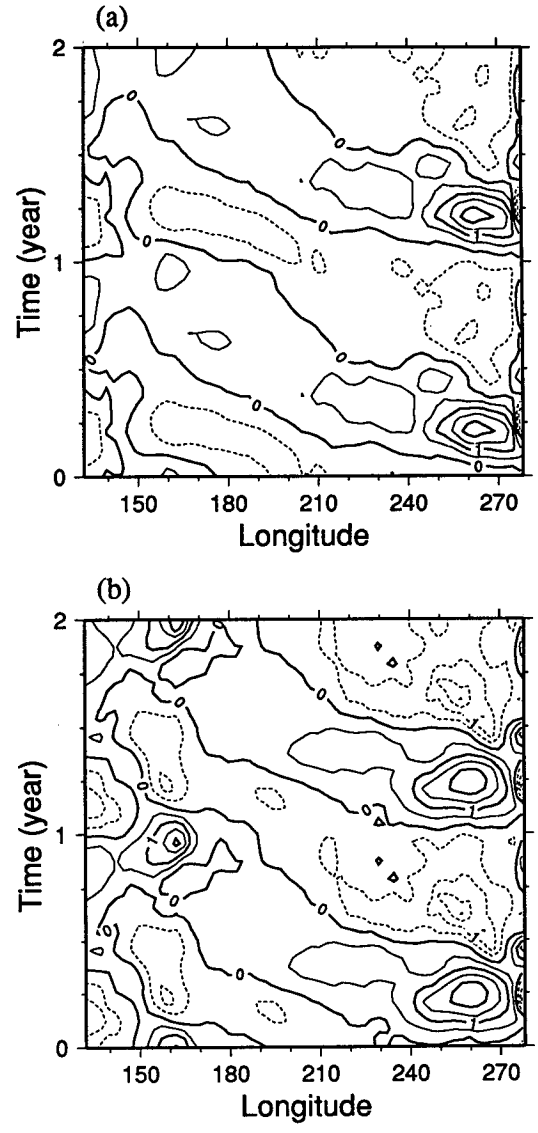

FIG. 7. Mean seasonal cycle of the uncoupled OGCM SST fields as a function of time and longitude along the equator (repeated twice). The ocean model is forced by observed seasonally varying wind stress and heat flux. SST averaged by calendar month is shown as anomalies with respect to the time mean over the last 4 yr of 9-yr and 6-yr runs, respectively. (a) For the case with the modified vertical mixing scheme; (b) as in (a) but for the case with the PP vertical mixing scheme. Contour interval is 0.5°C. Dashed lines represent negative anomalies.

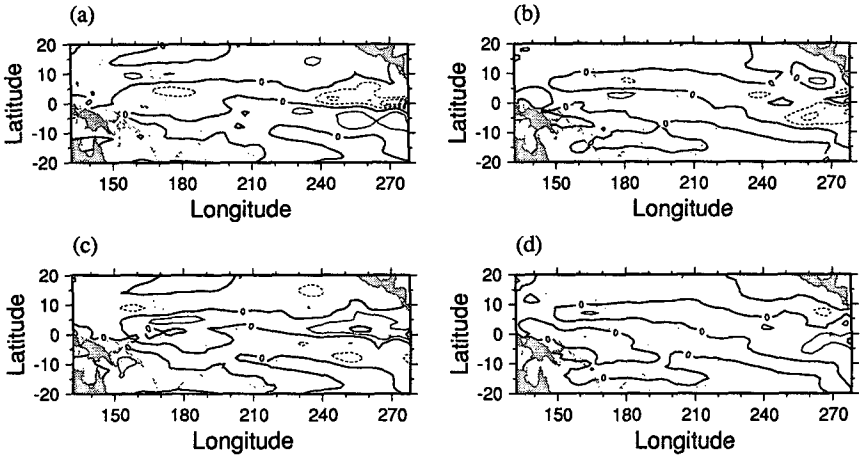

FIG. 8. Difference between the SST MSC for the uncoupled OGCM, with boundary conditions of seasonal-varying wind stress and heat flux, and the MSC for the OGCM integration, with boundary conditions of seasonally invariant wind stress and seasonally varying heat flux. The modified mixing scheme is employed in the OGCM. Seasonal averages are displayed, as a function of latitude and longitude, for (a) spring (MAM), (b) summer (JJA), (c) fall (SON), and (d) winter (DJF). Contour interval is 0.5°C and dashed lines represent negative values.

SST anomalies south of the equator are substantially a remote response to meridional wind stress variations north of the equator. The SST patterns are considerably more complex than those forced by a spatially constant meridional wind as in Philander and Pacanowski (1981).

5. Coupled seasonal cycle experiments

As outlined in section 2, coupling is carried out in two ways: experiments without the seasonal cycle and ones with "coupled seasonal cycle," in which the seasonal cycle includes momentum feedbacks with the wind stress simulated by the atmospheric model. Coupling begins from the end of the ocean climatology run, a near-stationary state with no seasonal cycle. Figure 9 shows the time–longitude distribution of the SST field along the equator over 21 years of the coupled seasonal cycle experiment (using the SVDAI atmospheric model). Because the annual-average climatology is no longer a stationary solution in the presence of seasonally changing heat flux, the system receives a gentle initial shock from the switch to January heat flux in year 0, after which it goes into a large spring warming. Over the next few years it establishes an equilibrium climatology, exhibiting both an annual cycle and interannual variability.

The longitudinal distribution of the warm pool and cold tongue along the equator is similar to the OGCM climatology. Strong variability with multiple frequencies, dominated by annual and quasi-biennial (QB) cycles, arises from coupled interactions. The irregularity in amplitude and structure is associated with lower-frequency variation. Additional hints of irregular variability are found in the sensitivity studies in section 7, although overall the oscillation is more regular than the observed ENSO.

a. The coupled seasonal cycle

Since the model results include both seasonal and interannual variations, these two phenomena are separated by taking the MSC and anomalies with respect to it. The simulated MSC of SST for the last 17 years (19 years for the case with the PP scheme) of the run is shown in Fig. 10a as a function of time and longitude along the equator, repeated twice with the time mean removed. In the eastern Pacific, the model seasonal cycle is comparable in amplitude to observations. Warm anomalies appear from December to June with maximum warming between February and April and are located a little off the eastern coast; these patterns actually provide an even better approximation to observations than the OGCM simulation (Fig. 7a), although this must be serendipitous. The model reproduces the prominent feature of westward propagation as seen in observations.

The associated MSC of zonal wind stress anomaly is shown in Fig. 10b. The seasonal cycle is of reasonable amplitude. The maximum wind stress anomalies, located in the central and eastern Pacific in agreement with observations, have a nonlocal relationship with the maximum SST anomalies, although the maximum easterly anomalies are shifted slightly eastward compared to observed. Off the equator, the SST and wind stress anomaly fields (figures not shown) also present reasonable distribution, amplitudes, and seasonal variations.

To further quantify the impact of these coupled momentum feedbacks in the seasonal cycle, we repeat the

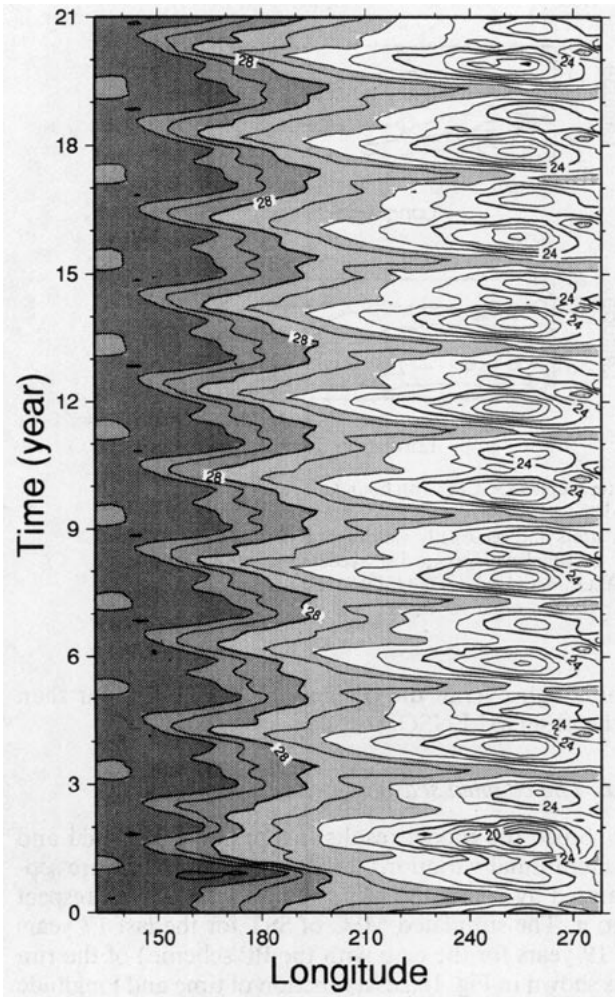

FIG. 9. Time–longitude distribution of the total SST field along the equator for the 21-yr coupled model simulation, with the modified vertical mixing scheme in the OGCM and the SVDAI atmosphere for the coupled seasonal cycle case, with coupling coefficient 1.0. Contour interval is 1°C. The light, medium, and heavy gray shadings represent SST higher than 26°, 28°, and 30°C, respectively.

estimation used in the uncoupled experiment in section 4. The departure of the coupled MSC is computed with respect to the uncoupled MSC, run with the boundary condition of seasonally varying heat flux but seasonally invariant wind stress. Figures 11a–d show the horizontal distribution of the SST departures as seasonal averages.

The impact of the momentum flux feedbacks in the coupled experiment successfully reproduces the effects of the specified momentum flux in the uncoupled experiment (Fig. 8). For example, the distribution of the cold and warm anomalies in the equatorial eastern Pacific shares similar patterns, although the momentum feedbacks give slightly stronger impact in the equatorial eastern Pacific south of the equator and slightly weaker impact in the equatorial western Pacific. The possibility that feedbacks among SST, wind stress, equatorial currents, and upwelling produce the observed westward propagation along the equator in the annual cycle has been raised by various investigators, particularly since westward-propagating "SST modes" in simple coupled models have suggestively similar properties (G. Philander 1990, personal communication; Neelin 1991; Chao and Philander 1993; Hao et al. 1993). While the wind stress feedbacks here do affect the form of the westward propagation of SST, a substantial contribution to the westward propagation actually comes from the heat flux. Thus, feedbacks among wind stress, SST, and ocean dynamics appear not to be sufficient to account for the westward propagation of the equatorial

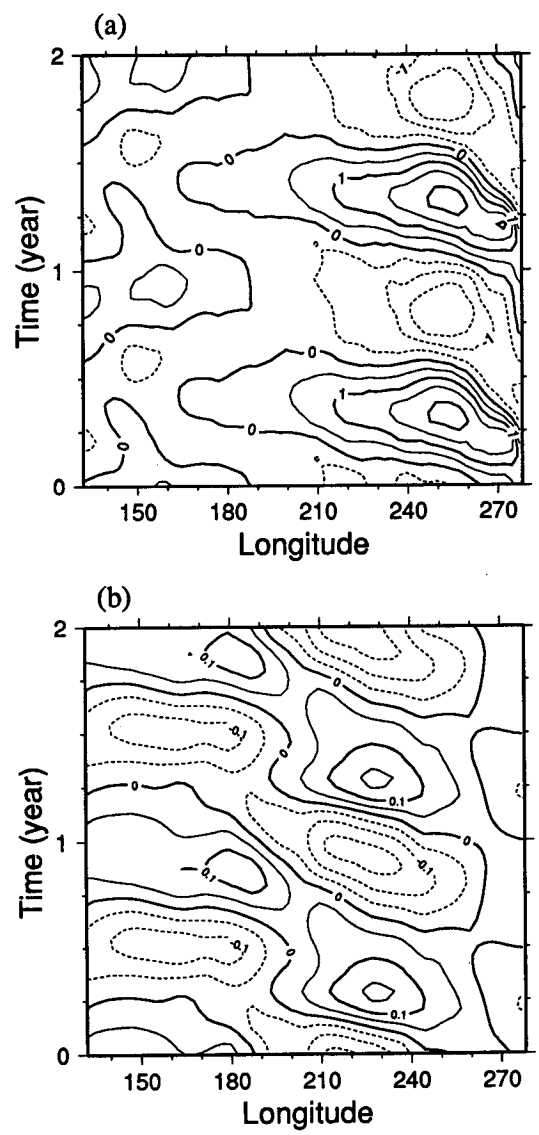

FIG. 10. Time–longitude distribution of the MSC of (a) SST and (b) zonal wind stress, repeated twice after the annual mean is removed, for the coupled model case in Fig. 9. Contour interval is 0.5°C for (a) and 0.05 dyne cm^{-2} for (b). Dashed lines represent negative anomalies.

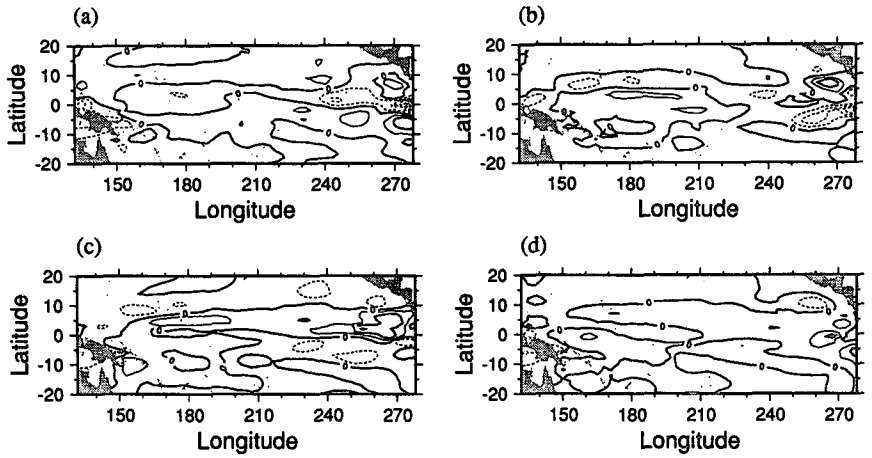

FIG. 11. Horizontal SST distribution as the difference between the MSC for the coupled model case in Fig. 9 and the MSC of the uncoupled OGCM integration that is forced by seasonally invariant wind stress and seasonally varying heat flux. The modified vertical mixing scheme is used. Seasonal averages are shown in (a) spring (MAM), (b) summer (JJA), (c) fall (SON), and (d) winter (DJF), with contour interval 0.5°C. Dashed lines represent negative values.

annual cycle. The meridional wind stress feedbacks do appear to be quite active in the annual cycle, as postulated for instance by Mitchell and Wallace (1992).

Figures 12a,b show zonal–vertical sections of the temperature field along the equator corresponding to Fig. 11, but for only fall and winter, with time mean removed. For comparison, Figs. 12c,d present the same analysis as in a,b but for the uncoupled ocean case. Spring and summer anomalies are very similar, but with the opposite sign, to fall and winter, respectively. Much of the seasonal variation is characterized by changes in the thermocline slope associated with westerly wind stress anomalies in winter and spring (easterly anomalies in summer and fall) that cause the thermocline to shoal (deepen) to the west. Coupled feedback and uncoupled cases are similar along the thermocline: for example, the phase, slope, and location of the maximum thermocline variation in the central and western Pacific. However, differences are found in the eastern Pacific around 240°E in the upper 100 m. This impact is also seen in the same analysis for SST in Fig. 11 south of the equator around 240°E and is probably associated with meridional wind stress feedbacks.

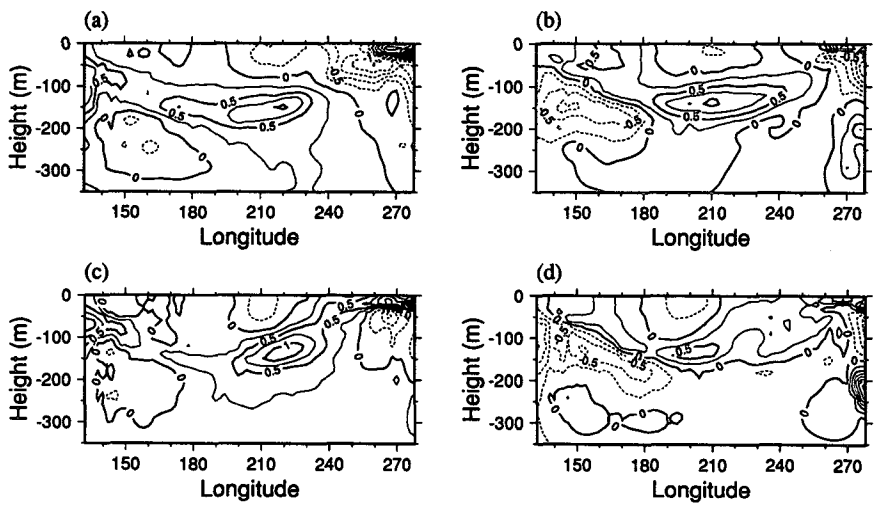

FIG. 12. (a) As in Fig. 11 but for the longitude–depth temperature field along the equator for fall. (b) As in (a) but for winter. (c) Same analysis as in (a) but for the uncoupled case in Fig. 8 for fall. (d) As in (c) but for winter. The time average has been removed. Contour interval is 0.25°C. Dashed lines represent negative values.

The coupled seasonal cycle of the run with the PP vertical mixing scheme (Fig. 13) gives quite different results. Although some success is obtained by the PP scheme (e.g., the westward propagation and comparable amplitudes in the eastern Pacific), several unrealistic features are also produced. The excessive SST anomaly variation in the western Pacific is notable and appears to be associated with the deficiencies found in the uncoupled OGCM simulation (see Fig. 7b), further exaggerated by the coupling. In a more detailed analysis, these excessive SST anomalies can be explained by the combination of maximum zonal current anomalies, strong activity of upwelling, and the large variation of vertical stratification in the western Pacific (figures not shown), which are caused by insufficient vertical mixing given by the PP scheme in the upper ocean. The resulting SST anomalies lead to wind stress feedbacks that reinforce these effects. With the modified vertical mixing scheme applied, which provides more mixing in the upper ocean, this feedback loop is interrupted, with attendant improvement (Fig. 10a).

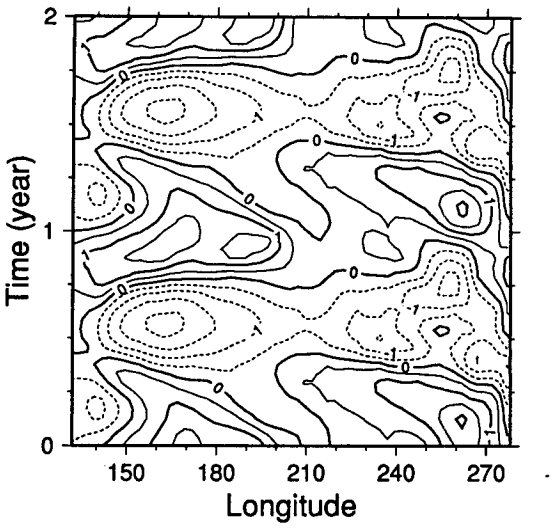

FIG. 13. As in Fig. 10a but for the coupled model case with the PP vertical mixing scheme.

b. Interannual variability

This subsection addresses the interannual variability in the coupled seasonal cycle experiment. Here, "anomaly" refers to "anomaly with respect to the MSC" unless otherwise specified. A quasi-biennial oscillation dominates the anomaly fields: although amplitudes and some details differ between warmings, the average period is very close to 2 years. A composite cycle is constructed by taking month-by-month means of each 2-yr period in the last 16 years of the run. Figures 14a–e present the composite time–longitude distributions of SST, zonal wind stress, heat content of the upper ocean (above 300-m depth), zonal current, and upwelling anomalies, respectively.

The SST anomaly field, which is positively correlated with heat content, westerly zonal wind, and eastward zonal current anomalies, and negatively correlated with upwelling anomalies, exhibits reasonable zonal distribution but weaker amplitudes compared to observations. The largest SST fluctuations occur in the eastern Pacific with 2°–3°C difference from the cold phase to the warm phase. SST variability in the western Pacific is slightly larger than observed interannual variability (about 1°C). The maximum warming tends to occur in winter, consistent with observations. During warm episodes, the heat content anomaly is positive in the east, showing the deepening of the thermocline, and less positive (or negative) in the west. The oscillation tends to have a locally standing character in both east and west. Deep thermocline (positive heat content anomaly) in the western Pacific leads deep thermocline and warm SST in the eastern Pacific by less than 180° of the phase of the oscillation, characterizing ocean dynamics that is not adjusted to earlier wind stress and thus contributes to the memory of the oscillation. The tendency of the western positive anomalies to connect to the subsequent eastern positive anomalies via a very slow eastward "propagation" is similar to the dynamics noted, for instance, by Cane and Sarachik (1981), Zebiak and Cane (1987), and Chao and Philander (1993). However, an obvious westward propagation is found in both SST and zonal wind stress anomaly fields. According to the intermediate model results discussed in Jin and Neelin (1993a,b) and Neelin and Jin (1993), all of these features are consistent with a regime of mixed SST–ocean-dynamics mode, where oscillation tendencies due to subsurface adjustment and westward propagation are combined. The onset of warm/cold SST in the eastern part of the basin corresponds closely to the subsurface warming/cooling (in-phase relationship), which is presented by the heat content anomaly. Although the wind stress is entirely determined by SST, the relationship between the patterns of evolution is not trivial, due to the nonlocal dependence.

The almost in-phase relationship between the zonal current and wind stress anomalies indicates a near-equilibrium response of the surface oceanic circulation to the atmospheric driving on the interannual timescale. In the vertical velocity field, downwelling anomalies driven by the westerly wind anomalies contribute to warming the SST in the western Pacific. In the eastern Pacific, upwelling anomalies appear less important.

A similar quasi-biennial oscillation is also found in the run with the PP scheme. The 2-yr composite SST anomaly of this run is presented in Fig. 15. Although the spatial features are quite similar in both runs, the temporal phase simulated by the PP scheme is shifted by roughly 3 months compared with the modified scheme as well as with observations. The modified scheme produces slightly weaker interannual variability while the MSC for both runs have comparable ampli-

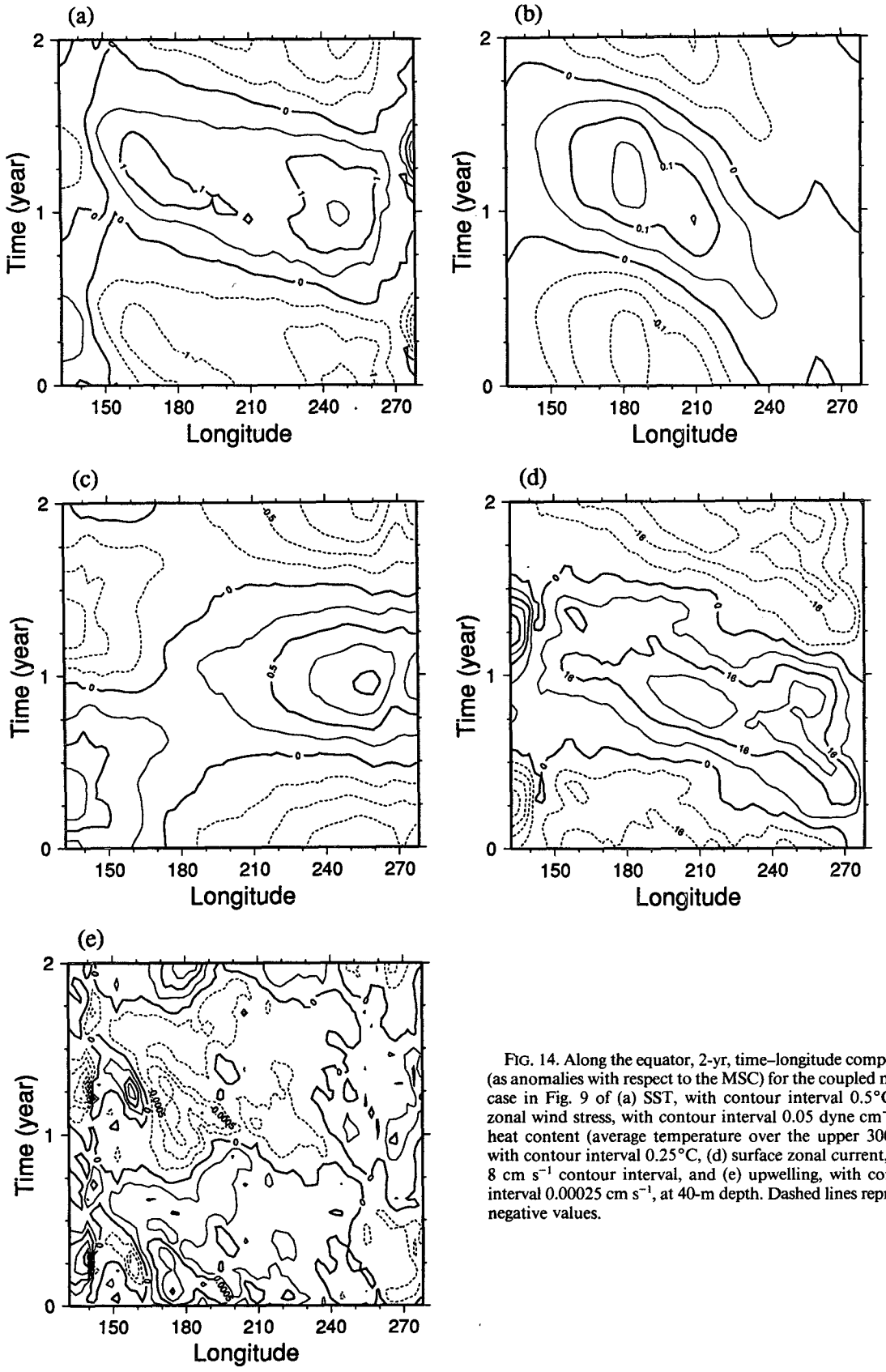

FIG. 14. Along the equator, 2-yr, time–longitude composites (as anomalies with respect to the MSC) for the coupled model case in Fig. 9 of (a) SST, with contour interval 0.5°C, (b) zonal wind stress, with contour interval 0.05 dyne cm^{-2}, (c) heat content (average temperature over the upper 300 m), with contour interval 0.25°C, (d) surface zonal current, with 8 cm s^{-1} contour interval, and (e) upwelling, with contour interval 0.00025 cm s^{-1}, at 40-m depth. Dashed lines represent negative values.

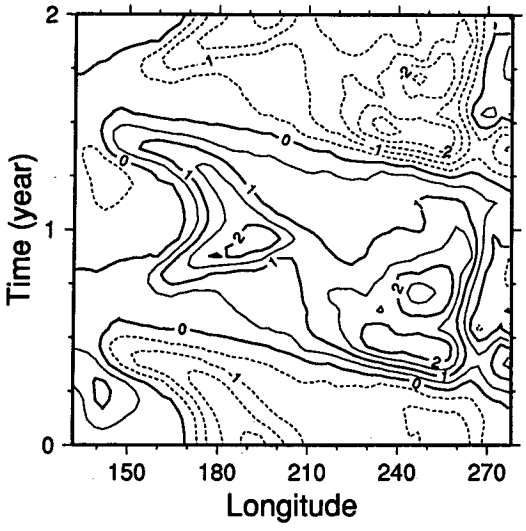

FIG. 15. As in Fig. 14a but for the coupled model case with the PP vertical mixing scheme.

tudes. The relatively large amplitude of variability near the date line with both schemes is associated with the warm SSTs in the western Pacific produced by the Oberhuber heat flux in the ocean model climatology. When mean SST is artificially constrained to observations, this variability is reduced.

Based on the 2-yr time–longitude SST anomaly composite with the modified scheme, maps of a cold phase [average over December, January, and February of the year before the "El Niño" year, DJF(−1)], a warm phase [DJF(0)], and two transition phases [JJA(0), transition from cold to warm phase, and JJA(+1), transition from warm to cold phase] are constructed, showing the temporal evolution of a complete El Niño–La Niña cycle. The composites of the SST anomaly field for the transition phase JJA[0] before the warm phase and the warm phase are displayed in Figs. 16a,b. The other transition phase [JJA(+1)] and the cold phase are almost identical to the phases shown but with the opposite sign.

A small positive SST anomaly first appears along the eastern boundary of the basin slightly south of the equator (Fig. 16a), while the remains of the preceding cold phase may still be seen in the western basin. The onset of the main warm anomalies (Fig. 16b) occurs rapidly across the basin associated with the subsurface warming seen in heat content (Fig. 14c). The positive anomaly develops up to 1.5°C in the eastern Pacific during the warm phase. The anomaly maximum then returns toward normal temperature and migrates farther west in the warm-to-cold transition phase. The onset and evolution of the subsequent cold phase have remarkably similar patterns except for the sign reversal. The behavior of the simulated SST field in the above scenario is in broad agreement with the development of composite anomalies associated with observed ENSO events documented by Rasmusson and Carpenter (1982) and Deser and Wallace (1990). The warm phase may be compared to Rasmusson and Carpenter's mature phase in terms of calendar month and to Deser and Wallace's December–February regression, although the meridional extension of the equatorial warm anomaly in our warm phase is narrower than observed. This is a feature shown by many models, including some GCMs (Mechoso et al. 1995) and uncoupled OGCMs. The reason for it is unclear. Because the development of the HCM ENSO cycle is faster than observed, the warm phase in our model simulation also catches certain features of what Rasmusson and Carpenter (1982) referred to as their "transition phase." Our transition phase is more comparable to that of Latif et al. (1993b).

The horizontal distributions of some critical quantities are displayed in Figs. 17a–d for the transition phase and Figs. 18a–d for the warm phase. During the transition phase, high heat content in the western equatorial region (Figs. 17c,d) is communicated eastward at depth along the equator, leading to a deepening equatorial thermocline to the east in the subsequent warm phase (Figs. 18c,d). The warm phase SST anomaly (Fig. 16b), almost in phase with the eastern equatorial heat content anomaly (Fig. 18d), reaches its maximum in the eastern Pacific along the equator.

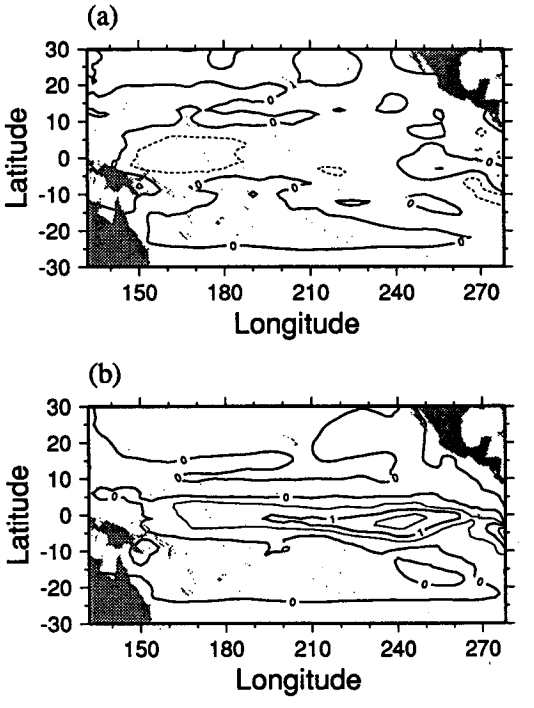

FIG. 16. Horizontal distribution of the SST anomaly composites for the coupled model case in Fig. 9. Two quadrature phases are displayed: (a) transition phase (from cold to warm) [JJA(0)], (b) warm phase [DJF(0)], with contour interval 0.5°C. Dashed lines represent negative anomalies.

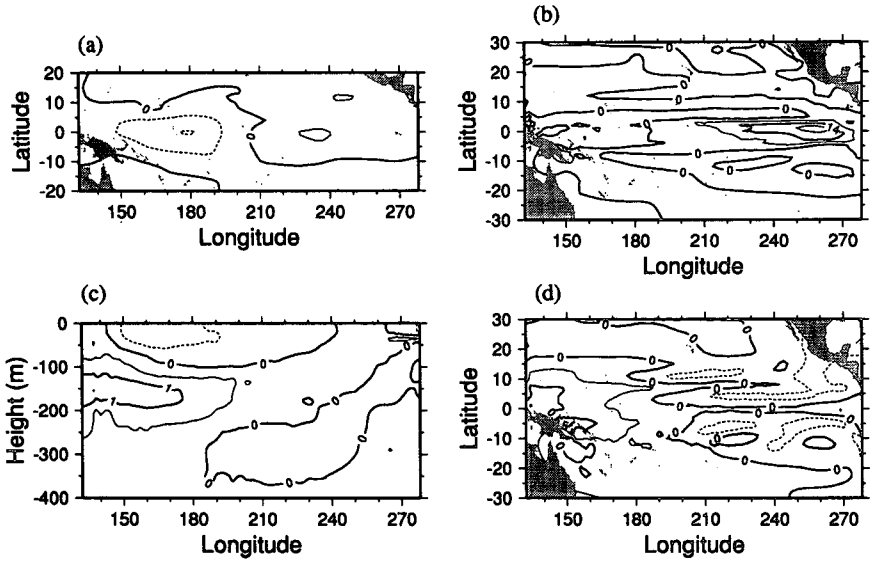

FIG. 17. Composite anomalies for the transition phase of (a) zonal wind stress, with 0.05 dyne cm^{-2} contour interval, (b) surface zonal current, with 7 cm s^{-1} contour interval, (c) longitude–depth temperature distribution along the equator, with 0.5°C contour interval, and (d) heat content (temperature averaged above 300 m), with 0.25°C contour interval.

The seed of the onset of the subsequent cold event is already seen by the subsurface structure (Figs. 18c,d) in the western Pacific during the warm phase. These fields are consistent, for instance, with the principal oscillation pattern analysis of the observed depth of the 20°C isotherm in Latif et al. (1993b), with slightly different phase normalization. The temperature increases at depth in the western Pacific while surface conditions are still cold (Fig. 17c). This may be compared to observations by Latif and Graham (1992).

The development of zonal wind stress anomalies is in agreement with the analysis in Rasmusson and Carpenter (1982). Westerly anomalies start to occupy the eastern half of the basin in the transition phase (Fig. 17a), while easterly anomalies are confined to the western half of the basin and weakened. Along with the intensification and extension to the west of westerly anomalies, negative SST anomalies are weakened in magnitude (transition phase, Fig. 16a) and positive anomalies develop to their largest magnitude in the

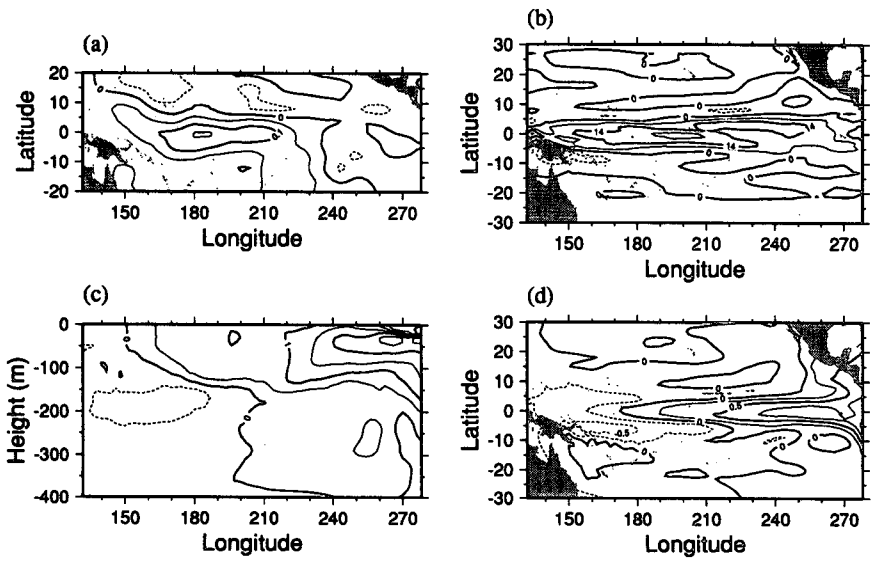

FIG. 18. As in Fig. 17 but for the warm phase.

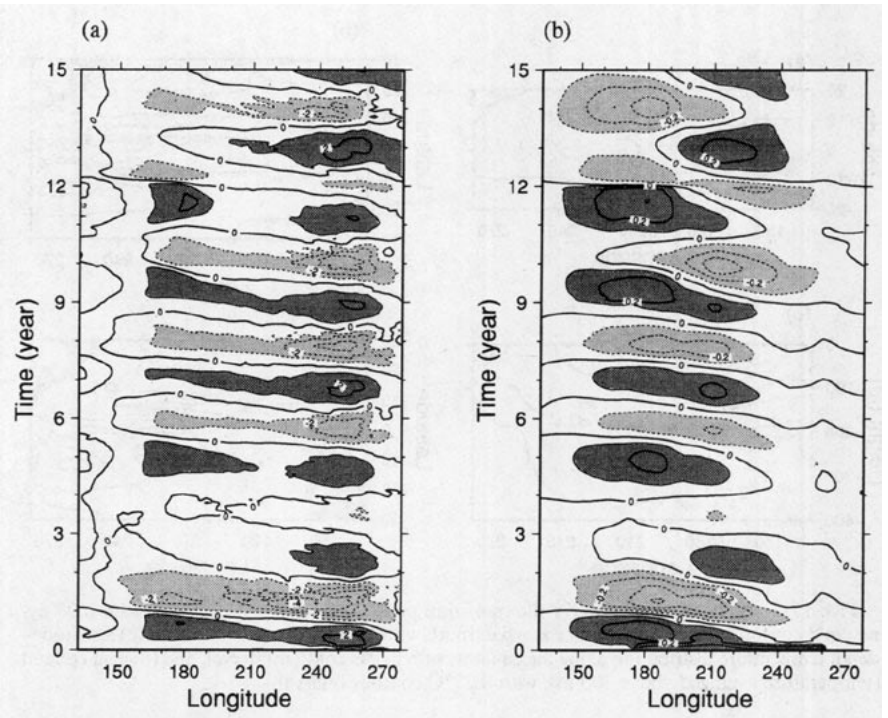

FIG. 19. Time–longitude diagrams, along the equator, for the coupled experiment (with the modified vertical scheme in the OGCM and the SVDAI atmospheric model) without the seasonal cycle. Anomalies (time mean removed) of (a) SST, with contour interval 1°C, (greater than 1°C shaded heavy gray, smaller than −1°C shaded light gray) and (b) zonal wind stress, with 0.1 dyne cm^{-2} contour interval, (greater than 0.1 dyne cm^{-2} shaded heavy gray, smaller than −0.1 dyne cm^{-2} shaded light gray) are displayed. Negative values are marked as dashed lines.

eastern Pacific in the warm phase (Fig. 16b). Wind-driven zonal current anomalies in the transition phase (Fig. 17b) show a pattern roughly comparable with local forcing of zonal wind anomalies, which also helps with the development of warm SST anomalies in the eastern Pacific.

In the warm phase, surface westerly wind anomalies prevail over the central and western part of the equatorial Pacific basin (Fig. 18a), dominated by the leading ENSO mode of the SVD analysis (see Fig. 3a). Both the eastward zonal current anomalies across the entire equator (Fig. 18b) and the equatorial heat content increase (Fig. 18d) clearly involve a remote and/or delayed response to the wind anomalies, with the thermocline depressed along the equator, especially in the eastern Pacific (Fig. 18c). The associated SST anomaly field (Fig. 16b) responds both to zonal advection flowing from the climatologically warm region in the western Pacific to the east, as well as to the vertical advection of increased subsurface temperature.

6. Inherent variability in the absence of the seasonal cycle

To understand the influence of the seasonal cycle in the coupled processes, it is useful to know the properties of the inherent variability in the absence of the seasonal cycle. Using annual-average boundary conditions excludes externally determined timescales and permits examination of the inherent ENSO frequency of the model without the frequency locking that tends to occur in the presence of the seasonal cycle. Two experiments corresponding to the two versions of the atmospheric model (SVDAI and SVDI) were conducted. While both models include interannual anomalies in the atmospheric response of the winds to SST, SVDI does not include any component associated with the spatial wind stress pattern of the annual cycle. A 0.3 dyne cm^{-2} initial westerly wind stress anomaly is applied for 1 month over the area from 180° to 260°E and 10°S to 10°N in both experiments without the seasonal cycle.

Figures 19a,b show the time–longitude distributions of anomalies (i.e., with time mean removed) of SST and zonal wind stress over 15 years as obtained from the coupled model with the SVDAI atmosphere in the absence of the seasonal cycle. Instead of the closely 2-yr-locked oscillations in the coupled seasonal cycle experiment (Figs. 9, 14a), the system shows an inherent period of 26 months. Irregular behavior is more obvious here than in the coupled seasonal cycle case. The spatial distribution of SST, wind stress, and other anomaly fields (e.g., heat content and vertical velocity

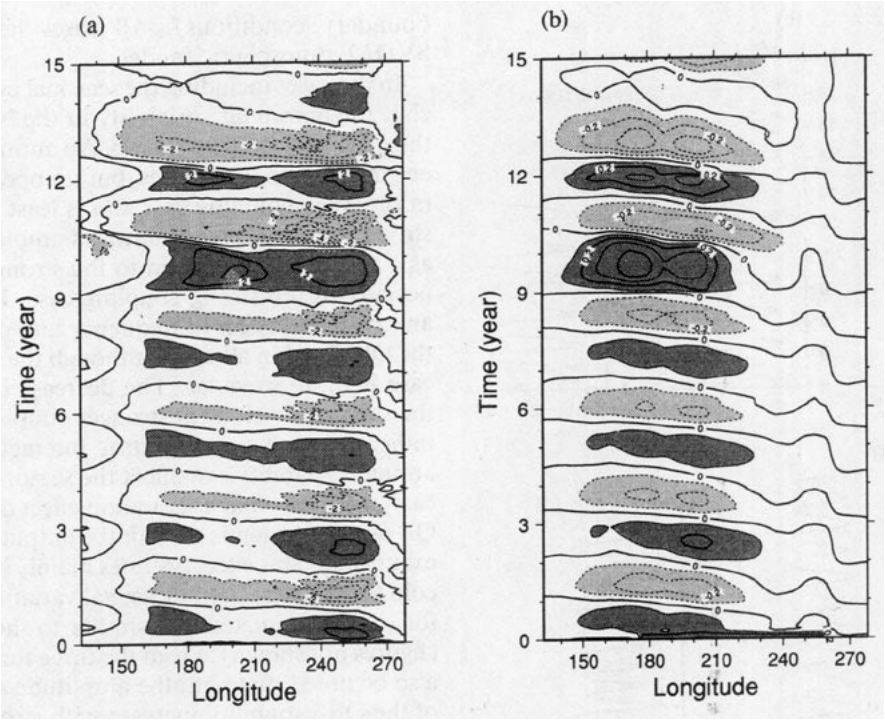

FIG. 20. As in Fig. 19 but for the coupled experiment with the SVDI atmospheric model.

anomalies, figures not shown) is quite similar, as is the phase relationship among them, showing that the oscillation is based on the same mechanism as in the case with the seasonal cycle.

Using the SVDI atmosphere produces oscillations similar to those with the SVDAI model, although the dominant period of 27.6 months is slightly longer (Figs. 20a,b). The spatial distribution and the temporal relationship among SST, wind stress, and other anomaly fields are very comparable to the SVDAI case. Thus, the inclusion of a spatial component in the atmospheric wind stress feedbacks that is normally associated with the seasonal cycle in the SVDAI model has little effect on the interannual oscillations when no seasonal forcing by heat flux is present.

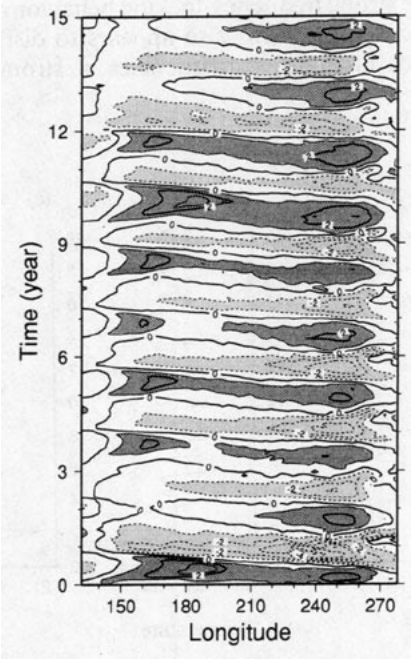

FIG. 21. As in Fig. 19a but for the case with the PP vertical mixing scheme.

Figure 21 illustrates the time series of SST anomalies for the SVDAI model when the PP scheme is employed. A corresponding run with the PP scheme and the SVDI model (not shown) behaves very similarly to this case with the SVDAI model, aside from a slight difference in period. The PP scheme tends to give shorter periods for the inherent interannual variability: 19 months for the SVDAI and 21 months for the SVDI model. The amplitude is also affected: with the PP scheme, stronger amplitudes in both the eastern and western Pacific are obtained. However, the spatial distribution and the temporal relationship among the SST field and other fields are generally similar to the cases with the modified mixing scheme. If we had run only cases with a specified seasonal cycle, we might never have noticed the problems with the PP scheme that emerged dramatically in the case of the coupled seasonal cycle.

7. Sensitivity studies

The coupled system has a sensitive dependence on parameters, of which one of the simplest and most im-

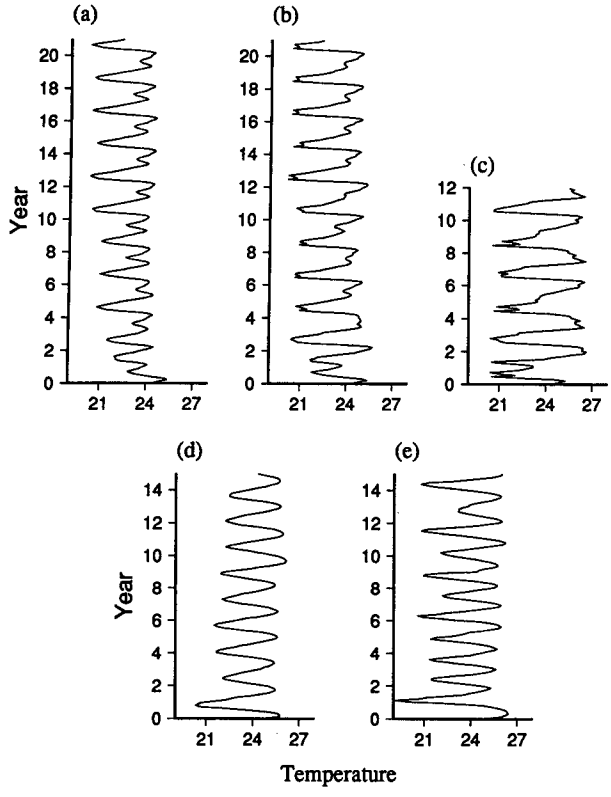

FIG. 22. Time series of NINO3 SST in the case of the PP vertical mixing scheme for the sensitivity studies (a) including the seasonal cycle at weak coupling (coupling coefficient 0.8); (b) as in (a) but at standard coupling (1.0); (c) as in (a) but at strong coupling (1.4); (d) for the interannual variability experiments without the seasonal cycle at standard coupling (1.0); (e) as in (d) but at strong coupling (1.4).

portant is the coupling strength, which we vary here. Interannual variability is usually easier to sustain for stronger coupling; very strong coupling can result in secondary bifurcations and even chaotic regimes (e.g., Münnich et al. 1991; Neelin 1990; Jin et al. 1994; Tziperman et al. 1994). As in the previous sections, two types of experiments, one with the seasonal cycle and the other one without, are carried out with the PP scheme and the modified scheme to contrast the nature of interannual variability about a time-invariant climate with that in the presence of the seasonal cycle.

Figure 22 illustrates the time series of SST for the NINO3 index region (averaged from 150°W to 90°W and from 5°S to 5°N) for experiments with the PP scheme. Upper panels represent the results of runs including the seasonal cycle, with coupling coefficient 0.8 (weak coupling), 1.0 (standard), and 1.4 (strong) displayed from left to right, respectively; lower panels are for experiments without the seasonal cycle, with the standard case presented on the left and the strong coupling case on the right. Each of the experiments is integrated for at least 12 years, starting from the same initial conditions (the end of the third-year ocean climatology run with the PP scheme with annual-average boundary conditions). All cases here involve the SVDAI atmospheric model.

In the cases including the seasonal cycle (upper panels), the dominant variability in the NINO3 region is the quasi-biennial oscillation. An annual signal is present in all three time series, but it appears most clearly in the weak coupling case and is least apparent in the strong coupling case. In terms of amplitude, it appears as a smaller modification to the strong QB signal, especially in the strong coupling case. However, it has an important effect in frequency and phase locking to the QB signal in all cases, although the strong coupling case is more irregular. The decrease in amplitude of the seasonal cycle with stronger coupling serves as an indication that the nonlinear interaction with interannual variability can affect the seasonal cycle. In this case, it appears that a saturation effect due to the strong QB oscillation tends to limit the amplitude of seasonal excursions. This effect operates mainly in the equatorial cold tongue region; the seasonal variation off the equator is well simulated and similar to the standard case (figures not shown). From the three time series, it may also be noted that both the amplitude and irregularity of the QB variability increase with stronger coupling.

In the experiments with purely interannual variability (i.e., without seasonal cycle, lower panels), a 19-month mode is found for the PP scheme at standard coupling. Multifrequency behavior, with dominant 16-month and 33-month periodicity, may be seen with an increased coupling coefficient, presumably due to period doubling. The mode that appears with an inherent frequency of 19 months is related to the frequency-locked QB signal in the presence of the seasonal cycle. The strong frequency-locking behavior when the seasonal cycle is present also appears to disfavor the appearance of multiple frequencies at stronger coupling.

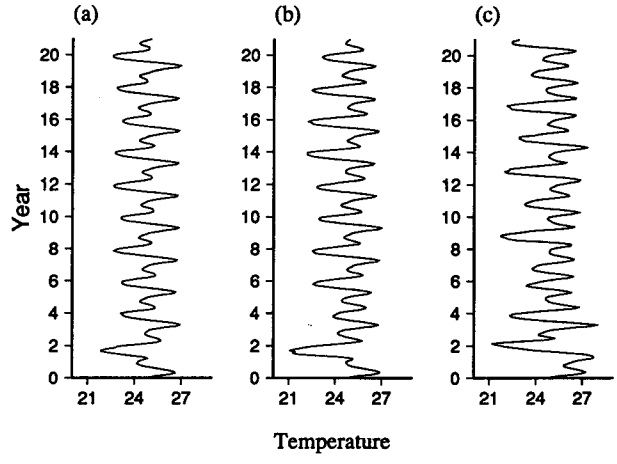

FIG. 23. As in Fig. 22a–c but for the case with the modified vertical mixing scheme at coupling coefficient (a) 1.0, (b) 1.2, and (c) 1.4.

The same NINO3 index analysis for coupled experiments with the modified vertical scheme in the presence of the seasonal cycle is displayed in Fig. 23 with coupling coefficient values 1.0, 1.2, and 1.4. Each of the experiments is integrated for 21 years, starting from the ocean climatology run described in section 4. Except for increased irregularity with stronger coupling, neither the interannual variability nor the coupled seasonal cycle are strongly affected by the increased coupling, although the amplitude of interannual variability is slightly increased with stronger coupling. Frequency locking of the seasonal cycle keeps the QB frequency dominant in all three cases. The spatial patterns among all experiments (with and without the seasonal cycle, with the PP and the modified scheme) are all quite similar.

8. Summary and discussion

A hybrid coupled model, consisting of an OGCM and an empirical atmospheric model for the wind stress response to SST, is used to simulate the seasonal cycle and ENSO interannual variability in the tropical Pacific. ENSO is widely recognized as resulting from ocean–atmosphere interactions; to investigate the hypothesis that similar coupled feedbacks play a role in the tropical seasonal cycle, we present an approach that models these feedbacks for the seasonal cycle on the same basis as for the interannual variability. Observed annual-average wind stress is specified by a flux-correction procedure, but the seasonal cycle of wind stress (the departure from annual average) is produced by the atmospheric model as part of a coupled response to the seasonal cycle of heat flux. This involves the response of SST both directly to the heat flux and to the momentum-flux feedbacks, which in turn depend on SST. This procedure could be applied with any atmospheric model that can simulate a reasonable seasonal cycle of wind stress in response to that of SST. Here it is applied using an empirical atmospheric model. A more conventional approach, in which only nonseasonal stress variability is included in the model atmosphere, is carried out in parallel.

The empirical atmospheric model is derived from the first seven coupled modes of a singular value decomposition (SVD) of the covariance between observed monthly mean surface wind stress and SST fluctuations. In the SVDAI (SVD–annual + interannual) version, anomalies of stress and SST are defined with respect to the long-term annual average, thus including both seasonal and interannual variability of stress and SST in the model. The first SVDAI mode describes the large-scale features of the 12-mo annual cycle, while the second and subsequent modes include a mixture of elements of the periodic seasonal cycle plus interannual variability. The SVDI (SVD–interannual) version of the empirical model is derived from observed anomalies defined with respect to the mean seasonal cycle and thus models only the nonseasonal wind response to SST. The spatial structure of the first SVDI mode is similar to that of the second SVDAI mode, and so on for the gravest SVDI modes.

Using these models with observed SST to reconstruct the coupled component of wind stress variability (i.e., that associated with SST) yields stress fields with timescales corresponding to slowly varying SST. The reconstructed stress fields capture roughly 90% of the observed low-frequency anomaly variance of stress within 10° of the equator, but a much smaller fraction of the observed variance at subannual timescales or away from the equator is described by either model, consistent with the contention that the empirical model is capturing only the coupled portion of the wind stress.

Experiments are conducted with two vertical mixing schemes, referred to as the PP scheme and the modified scheme. The coupled seasonal cycle experiment exhibits both seasonal and interannual variations. With the modified mixing scheme, the mean seasonal cycle shows reasonable characteristics compared with observations in amplitude and spatial pattern. The westward propagation of the SST anomaly field in the eastern Pacific is also well simulated. The results are compared to two uncoupled experiments: (i) an OGCM integration with the seasonal cycle specified in both heat flux and wind stress, and (ii) an OGCM integration with the seasonal cycle specified only in the heat flux, which would correspond to a coupling coefficient of zero being applied to the coupled seasonal cycle experiment. The differences of both coupled and uncoupled runs that include seasonal wind stress effects from the uncoupled case without these show that the coupled momentum feedbacks indeed have significant effects in producing the seasonal cycle, near the equator. However, wind stress feedbacks appear not to be the only factor producing westward propagation of SST anomalies along the equator. With the PP scheme, the uncoupled OGCM tends to produce excessive seasonal variations of SST in the western region (although with a pattern resembling the observed) due to the inefficient vertical mixing in this region given by the PP scheme; in the coupled model, the wind stress feeds back on these anomalies, thus increasing the error significantly.

The anomaly fields of the simulated El Niño cycle in the coupled seasonal cycle experiment are generally quite realistic in spatial characteristics and the phase relationship among the fields compared with observations, but with slightly weaker amplitudes. The largest SST variations occur in the eastern Pacific, in phase with the heat content anomalies, with peak-to-peak value of 2°–3°C. Maximum zonal wind stress anomalies appear in the central to western Pacific with an amplitude of 0.15–0.2 dyn cm^{-2} and are in phase with the maximum SST in the eastern Pacific. Heat content anomalies in the western Pacific lead by slightly less than half a cycle, prior to the deepening of the thermocline in the east that gives rise to the maximum SST

anomaly in the subsequent warm phase. SST and heat content fields in the eastern Pacific change essentially as a standing oscillation, indicating that ocean subsurface memory is dominant. Westward propagation is also seen in the SST field in the central basin and in the zonal wind stress field. Together with the 45°–90° phase differences in heat content between the eastern and the western Pacific, these features are very typical of the mixed SST–ocean dynamics regime, as noted in Jin and Neelin (1993a).

We find it particularly encouraging that we are able to obtain ENSO fluctuations of reasonable amplitude for realistic values of the wind stress feedback. A similar model by Barnett et al. (1993) required the wind stress to be multiplied by an artificial factor of 3 to get an ENSO cycle. We easily obtain an unstable ENSO mode for a modest drag coefficient $C_D = 1.2 \times 10^{-3}$. This is germane to current controversy (e.g., C. Penland and P. Sardeshmukh 1995, personal communication; Grieger and Latif 1994) over whether ENSO is an unstable mode or is maintained by noise.

When seasonal forcing is included, frequency and phase locking to a quasi-biennial (QB) period tends to dominate the temporal behavior. The model El Niños do not exactly repeat but the evolution is similar in each cycle. To understand this frequency locking, it is useful to examine the inherent variability of the system in the absence of the seasonal cycle. This inherent variability exhibits spatial form and temporal phase relations for the various fields that are very similar to the case with the annual cycle, strongly indicating that the model ENSO is based on the same mechanism with or without the annual cycle. This holds true with both SVDAI and SVDI versions of the atmospheric model. Thus, the inclusion of an atmospheric degree of freedom usually associated with the seasonal cycle in the coupled system has little effect on interannual oscillations in the absence of seasonal forcing. The SVDAI version produces a slightly shorter inherent period than the SVDI version, and both are somewhat longer than 2 years. With the PP mixing scheme, results are similar but the periods are shorter than 2 years with both atmospheric models. The inclusion of the seasonal cycle simply shifts the frequencies in all these cases to produce a 2-yr locked cycle.

Frequency locking has been noted in a number of other ENSO models (Anderson and McCreary 1985; Battisti 1988; Wu et al. 1993), including another HCM (Barnett et al. 1993). Jin et al. (1994) and Tziperman et al. (1994) recently demonstrated the close relationship between such frequency-locking behavior and the transition to chaos in intermediate and simple ENSO models, respectively. The locking tends to occur onto frequencies close to the inherent period, although integer periods, especially the biennial period, have a relatively broad parameter range. The intermediate model results of Jin et al. (1994), combined with the analysis of Jin and Neelin (1993a,b) and Neelin and Jin (1993), appear to apply in particular detail to the HCM results. In the intermediate model, the inherent frequency of the model ENSO was modified using a parameter (inversely related to momentum mixing) governing the strength of the surface-layer feedbacks. Quasi-biennial frequency locking occurred in the range where these feedbacks, involving vertical and zonal currents associated with vertical shear, were strong. In the HCM, with the PP mixing scheme, excessive anomalies of such currents appear to contribute to the westward extension of SST anomalies, apparently due to insufficient vertical mixing in near-surface layers. The tendency to westward propagation is also characteristic of slightly strong surface-layer feedbacks. The increase in period associated with the modified scheme seems consistent with the intermediate model results.

Jin et al. (1994) also note that biennial frequency-locking behavior occurs by both linear and nonlinear mechanisms, whereas frequency locking to other periods (e.g., 3 or 4 yr) is a nonlinear phenomenon. Thus, it tends to be more difficult to escape from a biennial-locked regime by simply increasing the amplitude of the interannual signal (e.g., by increasing the relative coupling coefficient). On the other hand, relatively small modifications that further increase the inherent ENSO period are likely to lead to a regime characterized by frequency locking to lower frequencies and to chaotic regimes. The challenge is to obtain these by physically realistic modifications in the HCM, such as further examination of the vertical mixing parameterization or surface heat flux parameterization.

In many ENSO models, including the intermediate and hybrid models mentioned above, the seasonal cycle is constructed by flux correction. Modifications to the constructed cycle by nonlinear interaction with interannual variability thus tend to be small and are difficult to interpret. Jin et al. (1994) note that the physics of frequency locking tends to involve nonlinearities in upwelling and thermocline depth, the seasonal cycle of which is most directly affected by wind stress. It is significant that similar frequency locking is produced in this model, where the seasonal cycle enters only in the heat flux and the seasonal wind stress is part of the response. This suggests that the models with flux-corrected seasonal wind stress are qualitatively correct in this behavior.

Examination of the joint behavior of the coupled seasonal cycle and ENSO variability as a function of coupling strength shows a more complicated dependency than anticipated. Because the results at standard coupling indicate that the wind stress feedbacks contribute to the coupled seasonal cycle along the equator, one might expect that the amplitude of both the seasonal cycle and the ENSO signal would increase with coupling. Instead, in the version with the PP scheme, the annual signal in the NINO3 SST index region is actually reduced at strong coupling by saturation effects caused by the strong interannual signal. On the other

hand, with the modified scheme, increased coupling strength does not affect the coupled seasonal cycle significantly, although the irregularity of interannual variability increases. Simulating the seasonal cycle on the same basis as interannual variability thus provides much stronger constraints on subgrid-scale parameterizations than simulating ENSO alone.

Acknowledgments. This work was supported in part by National Oceanography and Atmosphere Administration Grants NA46GP0244 and NA26GP0114 and National Science Foundation Grant ATM-92150900/9521389 (HHS and JDN). During completion of this paper, JDN was supported by the Henry G. Houghton lectureship and the Department of Earth, Atmospheric and Planetary Sciences at M.I.T. Computations were carried out at the National Center for Atmospheric Research, which is sponsored by NSF, and at The Florida State University Computer Center, sponsored by the NOAA Climate and Global Change Program. DSG is supported by the U.S. TOGA Program Office under NOAA Contract NA16RC0236-01 and by the NOAA EPOCS Program. We thank the NOAA Climate Analysis Center for providing the SST data and The Florida State University for pseudostress data. The authors thank R. Pacanowski, A. Rosati, and K. Dixon for providing a prerelease version of the GFDL MOM code, B. Blanke for providing the modified mixing and solar penetration schemes, W. Weibel for computational assistance, and F.-F. Jin and M. Latif for discussions. An earlier version of a portion of this work appeared in the Proceedings of the *Fourth Symposium on Global Change Studies,* sponsored by the American Meteorological Society in 1993.

APPENDIX A

Surface Heat Flux Parameterization

Oberhuber (1988) uses a surface heat flux of the form

$$Q_{\text{model}} = Q_{\text{obs}} + \alpha(T_{\text{obs}} - T_{\text{model}}),$$

where α is intended to approximate $-(\partial Q/\partial T)_{\text{obs}}$.

Following Seager et al. (1988), the negative feedback coefficient is approximated here by

$$\alpha = \rho_a C_D L |V|(1 - \delta)\left[\frac{dq_s(T)}{dT}\right]_{\text{obs}} + \alpha_{\text{SHLW}}$$

$$|V| \geq 4.5 \text{ m s}^{-1},$$

where Q is net surface heat flux, T is sea surface temperature, ρ_a is air density, C_D is the drag coefficient (1.2×10^{-3}), V is wind speed, α_{SHLW} is the combined effects of sensible heat and longwave radiation fluxes, set to a constant -1.5 W m^{-2} K^{-1}, and q_s is the saturation specific humidity. The factor δ is similar to relative humidity but measures the specific humidity of near-surface air q_a relative to the saturation value at the sea surface temperature; a value of 0.73 is used, as estimated from COADS data for the region of the tropical Pacific domain from -20°S to 20°N. The Oberhuber estimate of α differs principally in that no variation of q_a is assumed (i.e., $\delta = 0$); Oberhuber also uses a more complex formula for α_{SHLW}. Figure A1 shows the resulting distribution of the negative feedback coefficient.

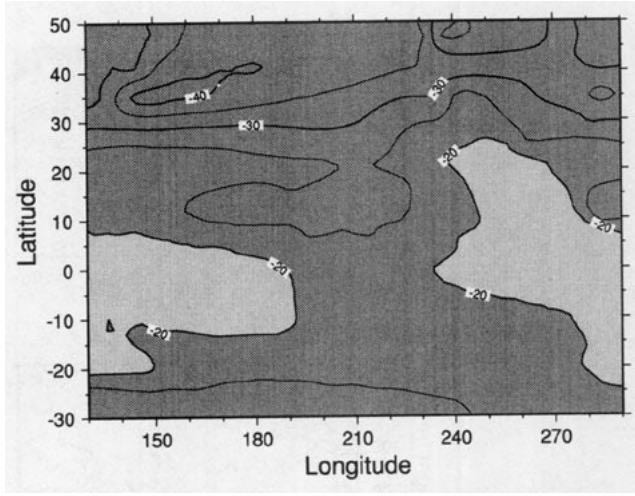

FIG. A1: The horizontal distribution of the heat flux negative feedback coefficient, estimated using the Seager et al. (1988) parameterization. Beyond ±20° this coefficient is blended with that estimated by Oberhuber (1988) over a linear blending region to ±30°. Contour interval is 5 W m^{-2} K^{-1}. Heavily (lightly) shaded areas represent those values less (greater) than -20 W m^{-2} K^{-1}.

APPENDIX B

Ocean Model Climatology

Figure B1a shows the horizontal SST distribution of ocean climatology. The extent of the warm pool in the western Pacific corresponds approximately to the observed annual-average pattern. The warmest SST is slightly greater than observed, probably due to our heat flux parameterization mentioned in section 2. In the eastern Pacific, the equatorial cold tongue is slightly colder than observed and it extends farther west, but still within a reasonable range. Although the simulated horizontal SST gradient is stronger than observed values both east and west of the 28°C isotherm, the position of this isotherm is realistic.

Examining the surface zonal currents (Fig. B1b), the north equatorial countercurrent and the south equatorial current have positions and extents in general agreement with measurements but have weaker magnitudes. Figure B1c shows the equatorial upwelling in a longitude–depth slice along the equator. The upwelling extends horizontally in a broad area as far west as 165°E, which may explain the equatorial cold tongue extending too far west. Although data are lacking for upwelling, both the vertical and horizontal extension of the upwelling, with the maximum occurring around

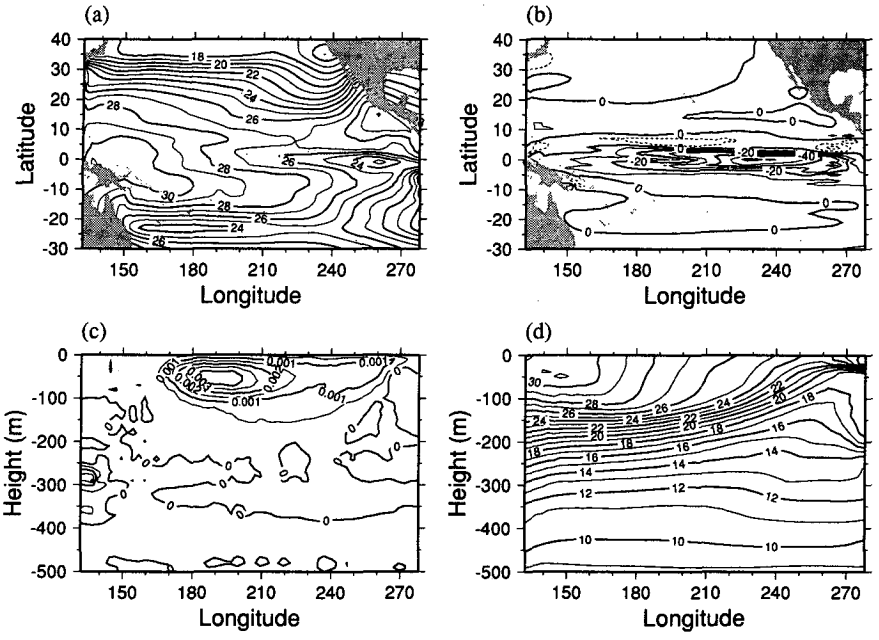

FIG. B1: Ocean climatology, defined as the average of the ninth year of the uncoupled OGCM integration with the modified vertical mixing scheme, forced with annual average climatological observed wind stress and heat flux. Horizontal distribution of (a) SST, with 1°C contour interval, and (b) surface zonal current, with 10 cm s^{-1} contour interval (solid lines represent westward currents); longitude–depth distribution along the equator of (c) upwelling, with 0.0005 cm s^{-1} contour interval (solid lines represent upwelling), and (d) temperatures, with 1°C contour interval, along the equator.

the depth of 50 m, compares well with the model results of Philander et al. (1987). However, the strength of upwelling is weaker compared with the same model when run with the PP scheme. In the cold tongue region where upwelling contributes the most to the cold SST, the strength of upwelling is about half as strong as the results obtained with the PP scheme.

The longitude–depth thermocline structure is displayed in Fig. B1d. The depth of the thermocline and the vertical gradient in the thermocline are quite realistic. The vertical temperature gradient above the thermocline in the western Pacific is also comparable with observations, while the PP scheme has stronger stratification in this region.

REFERENCES

Anderson, D. L. T., and J. P. McCreary, 1985: Slowly propagating disturbances in a coupled ocean–atmosphere model. *J. Atmos. Sci.*, **42**, 615–629.

Barnett, T. P., M. Latif, N. Graham, M. Flügel, S. Pazan, and W. White, 1993: ENSO and ENSO-related predictability. Part I: Prediction of equatorial Pacific sea surface temperature with a hybrid coupled ocean–atmosphere model. *J. Climate*, **6**, 1545–1566.

Battisti, D. S., 1988: The dynamics and thermodynamics of a warming event in a coupled atmosphere–ocean model. *J. Atmos. Sci.*, **45**, 2889–2919.

Blanke, B., and P. Delecluse, 1993: Variability of the tropical Atlantic Ocean simulated by a general circulation model with two different mixed layer physics. *J. Phys. Oceanogr.*, **23**, 1363–1388.

Bretherton, C. S., C. Smith, and J. M. Wallace, 1992: An intercomparison of methods for finding coupled patterns in climate data. *J. Climate*, **5**, 541–560.

Cane, M. A., and E. S. Sarachik, 1981: The response of a linear baroclinic equatorial ocean to periodic forcing. *J. Mar. Res.*, **39**, 651–693.

——, and S. E. Zebiak, 1985: A theory for El Niño and the Southern Oscillation. *Science*, **228**, 1084–1087.

Cattell, R. B., 1966: The scree test for a number of factors. *Multivariate Behavioral Res.*, **1**, 245–276.

Chao, Y., and S. G. H. Philander, 1993: On the structure of the Southern Oscillation. *J. Climate*, **6**, 450–469.

Cox, M. D., 1984: A primitive equation, 3-dimensional model of the ocean. GFDL Ocean Group Tech. Rep. No. 1, GFDL/NOAA.

Deser, C., and J. M. Wallace, 1990: Large-scale atmospheric circulation features of warm and cold episodes in the tropical Pacific. *J. Climate*, **3**, 1254–1281.

Gill, A. E., 1985: Elements of coupled ocean–atmosphere models for the tropics. *Coupled Ocean–Atmosphere Models*, Elsevier Oceanogr. Ser., Vol. 40, Elsevier, 303–328.

Graham, N. E., J. Michaelson, and T. P. Barnett, 1987: An investigation of the El Niño–Southern Oscillation cycle with statistical models, Part 1: Predictor field characteristics. *J. Geophys. Res.*, **92**, 14 251–14 270.

Grieger, B., and M. Latif, 1994: Reconstruction of the El Niño attractor with neural networks. *Climate Dyn.*, in press.

Gutzler, D. S., 1993: Modes of large-scale ocean–atmosphere interaction in the tropical Pacific. *Proc. 17th Annual NOAA Climate Diagnostics Workshop*, Norman, OK, Natl. Ocean. Atmos. Admin., 77–80. (NTIS PB93-183895.)

Halpert, M. S., and C. F. Ropelewski, 1989: *Atlas of Tropical Sea Surface Temperature and Surface Winds.* Climate Analysis Center, National Meteorological Center, National Weather Service.

Hao, Z., J. D. Neelin, and F.-F. Jin, 1993: Nonlinear tropical air–sea interaction in the fast-wave limit. *J. Climate,* **6,** 1523–1544.

Hirst, A. C., 1986: Unstable and damped equatorial modes in simple coupled ocean–atmosphere models. *J. Atmos. Sci.,* **43,** 606–630.

Horel, J. D., 1982: The annual cycle in the tropical Pacific atmosphere and ocean. *Mon. Wea. Rev.,* **110,** 1863–1878.

Jin, F.-F., and J. D. Neelin, 1993a: Modes of interannual tropical ocean–atmosphere interaction—a unified view. Part I: Numerical results. *J. Atmos. Sci.,* **50,** 3477–3503.

——, and ——, 1993b: Modes of interannual tropical ocean–atmosphere interaction—a unified view. Part III: Analytical results in fully coupled cases. *J. Atmos. Sci.,* **50,** 3523–3540.

——, ——, and M. Ghil, 1994: El Niño on the "Devil's Staircase": Annual subharmonic steps to chaos. *Science,* **264,** 70–72.

Latif, M., and A. Villwock, 1990: Interannual variability as simulated in coupled ocean–atmosphere models. *J. Mar. Systems,* **1,** 51–60.

——, and N. E. Graham, 1992: How much predictive skill is contained in the thermal structure of an OGCM? *J. Phys. Oceanogr.,* **22,** 951–962.

——, A. Sterl, E. Maier-Reimer, and M. M. Junge, 1993a: Climate variability in a coupled GCM. Part I: The tropical Pacific. *J. Climate,* **6,** 5–21.

——, ——, ——, and ——, 1993b: Structure and predictability of the El Niño/Southern Oscillation phenomenon in a coupled ocean–atmosphere general circulation model. *J. Climate,* **6,** 700–708.

Legler, D. M., 1983: Empirical orthogonal function analysis of wind vectors over the tropical Pacific region. *Bull. Amer. Meteor. Sci.,* **64,** 234–241.

——, and J. J. O'Brien, 1984: *Atlas of Tropical Pacific Wind-Stress Climatology 1971–1980.* The Florida State University, 182 pp.

Levitus, S., 1982: *Climatological Atlas of the World Ocean.* NOAA, U.S. Government Printing Office, 173 pp., 17 microfiche.

Mechoso, C. R., A. W. Robertson, and Coauthors, 1995: The seasonal cycle over the tropical Pacific in general circulation models. *Mon. Wea. Rev.,* **9,** 2825–2838.

Meehl, G. A., 1990: Seasonal cycle forcing of El Niño–Southern Oscillation in a global coupled ocean–atmosphere GCM. *J. Climate,* **3,** 72–98.

Mitchell, T. P., and J. M. Wallace, 1992: The annual cycle in equatorial convection and sea surface temperature. *J. Climate,* **5,** 1140–1156.

Münnich, M., M. A. Cane, and S. E. Zebiak, 1991: A study of self-excited oscillations in a tropical ocean–atmosphere system. Part II: Nonlinear cases. *J. Atmos. Sci.,* **48,** 1238–1248.

Neelin, J. D., 1990: A hybrid coupled general circulation model for El Niño studies. *J. Atmos. Sci.,* **47,** 674–693.

——, 1991: The slow sea surface temperature mode and the fast-wave limit: Analytic theory for tropical interannual oscillations and experiments in a hybrid coupled model. *J. Atmos. Sci.,* **48,** 584–606.

——, and F.-F. Jin, 1993: Modes of interannual tropical ocean–atmosphere interaction—a unified view. Part II: Analytical results in the weak-coupling limit. *J. Atmos. Sci.,* **50,** 3504–3522.

Nigam, S., and H.-S. Shen, 1993: Structure of oceanic and atmospheric low-frequency variability over the tropical Pacific and Indian Oceans. Part I: COADS observations. *J. Climate,* **6,** 657–676.

O'Lenic, E. A., and R. E. Livezey, 1988: Practical considerations in the use of rotated principal component analysis (RPCA) in diagnostic studies of upper-air height fields. *Mon. Wea. Rev.,* **116,** 1682–1689.

Oberhuber, J. M., 1988: An atlas based on the COADS data set: The budgets of heat buoyancy and turbulent kinetic energy at the surface of the global ocean. Max-Planck-Institut für Meteorologie Report No. 15,

Penland, C., and P. D. Sardeshmukh, 1995: The optimal growth of tropical sea surface temperature anomalies. *J. Climate,* **8,** 1999–2024.

Peters, H., M. C. Gregg, and J. M. Toole, 1988: On the parameterization of equatorial turbulence. *J. Geophys. Res.,* **93,** 1199–1218.

Philander, S. G. H., and R. C. Pacanowski, 1980: The generation of equatorial currents. *J. Geophys. Res.,* **85,** 1123–1136.

——, and ——, 1981: The oceanic response to cross-equatorial winds (with application to coastal upwelling in low-latitudes). *Tellus,* **33,** 201–210.

——, T. Yamagata, and R. C. Pacanowski, 1984: Unstable air–sea interactions in the tropics. *J. Atmos. Sci.,* **41,** 604–613.

——, W. J. Hurlin, and A. D. Siegel, 1987: Simulation of the seasonal cycle of the tropical Pacific Ocean. *J. Phys. Oceanogr.,* **17,** 1986–2002.

——, R. C. Pacanowski, N. C. Lau, and M. J. Nath, 1992: Simulation of ENSO with a global atmospheric GCM coupled to a high-resolution, tropical Pacific ocean GCM. *J. Climate,* **5,** 308–329.

Rasmusson, E. M., and T. H. Carpenter, 1982: Variations in tropical sea surface temperature and surface wind fields associated with the Southern Oscillation/El Niño. *Mon. Wea. Rev.,* **110,** 354–384.

Reynolds, R. W., 1988: A real-time global sea surface temperature analysis. *J. Climate,* **1,** 75–86.

Schopf, P. S., and M. J. Suarez, 1988: Vacillations in a coupled ocean–atmosphere model. *J. Atmos. Sci.,* **45,** 549–566.

Seager, R., S. E. Zebiak, and M. A. Cane, 1988: A model of the tropical Pacific sea surface temperature climatology. *J. Geophys. Res.,* **93,** 1265–1280.

Tziperman, E., L. Stone, M. Cane, and H. Jarosh, 1994: El Niño chaos: Overlapping of resonances between the seasonal cycle and the Pacific ocean–atmosphere oscillator. *Science,* **264,** 72–74.

Waliser, D. E., B. Blanke, J. D. Neelin, and C. Gautier, 1995: Shortwave feedbacks and ENSO: Forced ocean and coupled ocean–atmosphere experiments. *J. Geophys. Res. Oceans,* 25 109–25 125.

Wallace, J. M., T. P. Mitchell, and C. Deser, 1989: The influence of sea-surface temperature on surface wind in the eastern equatorial Pacific: Seasonal and interannual variability. *J. Climate,* **2,** 1492–1499.

Wu, D.-H., D. L. T. Anderson, and M. K. Davey, 1993: ENSO variability and external impacts. *J. Climate,* **6,** 1703–1717.

Zebiak, S. E., 1990: Diagnostic studies of Pacific surface winds. *J. Climate,* **3,** 1016–1031.

——, and M. A. Cane, 1987: A model El Niño–Southern Oscillation. *Mon. Wea. Rev.,* **115,** 2262–2278.